sciendo Powder Metallurgy Progress, Vol.19 (2019), No.1, p.001-011
http://dx.doi.org/10.1515/pmp-2019-0001

INFLUENCE OF SODIUM ALGINATE ON PROPERTIES OF TETRACALCIUM PHOSPHATE/ NANOMONETITE BIOCEMENT

R. Štulajterová, L. Medvecký, M. Giretová, T. Sopčák, J. Briančin

Abstract

The tetracalcium phosphate/nanomonetite (TTCPMH) biocements with the addition of sodium alginate were prepared by mechanical homogenization of powder mixture with hardening liquid containing sodium alginate. The effect of various viscosity of different alginates on properties of TTCPMH cement mixture was investigated. The medium viscous (MED) alginate had a more negative effect on setting process and compressive strength than low viscous (LOW) alginate. An approx. 50% decrease in mechanical properties (compressive strengths, Young´s modulus, work of fracture (WOF)) was revealed after an addition of 0.25 wt % with rapid fall above 1 wt % of LOW alginate in biocement. A statistically significant difference in the WOF was found between of 0.25 and 0.5 LOW alginate biocements ($p<0.035$) whereas no statistical differences were revealed between WOF of 0.5 and 1 LOW alginate biocements ($p>0.357$). In the microstructure of composite cements, the increased amounts of granular or finer needle-like nanohydroxyapatite particles arranged into the form of more separated spherical agglomerates were observed. A low cytotoxicity of cement extracts based on measurement of cell proliferation was revealed.

Keywords: polymeric additive (sodium alginate), tetracalcium phosphate/nanomonetite biocement, mechanical properties, composites, bioactivity

INTRODUCTION

Hydrogels are three-dimensional, hydrophilic, polymeric networks capable of absorbing large amounts of water or biological fluids. They can be chemically stable or degrade with disintegration and dissolution. The calcium phosphate cements have been widely investigated in view of their favorable handling properties. Many calcium phosphate cements (CPC) pastes tend to disintegrate upon early contact with blood or other aqueous body fluids, which limit the use of these materials in clinical practice such as bone repair, reconstruction and regeneration. For prevention of insufficient cohesion, the cohesion promotors such as sodium alginate are added [1]. The free cement particles may leak into the tissues surrounding, causing side effects - nerve pain, venous and pulmonary embolism [2].

Radoslava Štulajterová, Ľubomír Medvecký, Mária Giretová, Tibor Sopčák: Institute of Materials Research of SAS, Watsonova 47, 040 01 Kosice, Slovak Republic
Jaroslav Briančín: Institute of Geotechnics of SAS, Watsonova 45, 040 01 Kosice, Slovak Republic

The sodium alginate belongs to the group of water-soluble polymers which are non-toxic and widely used in various pharmaceutical and biomedical applications and therefore do not require removal from the system [3]. The alginate scaffolds lack in mechanical strength and fast hydrolyse which diminish applicability in bone tissue engineering. The mechanical properties of alginate scaffolds have been improved by mixing with calcium phosphates like hydroxyapatite (HA). Besides, the addition of HA to the alginate polymer enhanced the cell adhesion and proliferation on the scaffolds with an average pore size of 150 μm and over 82% of porosity [4]. Alginates are ion-sensitive natural hydrogels and they gel through chelation with divalent cations [5]. A crosslinking reaction occurs between sodium alginate and calcium released by CPC during setting, resulting in the formation of water-insoluble calcium alginate gel [6]. It has been shown that the cohesion and cement toughness of CPC pastes (based on α-TCP and liquid phase NaH2PO4.2H2O) was improved by the addition of polymeric additives (i.e. carboxymethylcellulose (CMC) and hyaluronan (HA)) [7]. The carboxyl group of this polymer provides the possibility to form electrostatic interactions with calcium ions in the CPC matrix [8]. The biopolymers primarily include degradable components such as chitosan, gelatin, collagen, and synthetic polymer phases [9-15]. CPC composites with various biopolymers (gelatin, collagen, chitosan, alginate) were studied for modification of their properties. Incorporation of sodium alginate, as a liquid phase, to calcium phosphate cement (TTCP/DCPA) caused the increase of setting time [6]. Similar results were found in the case of alginate/CPC composites composed of MCPM-CaCO3 [16] or ACP-DCPD [17]. It was reported the reduction in mechanical properties when the amount of sodium alginate in TTCP/DCPA cement exceeded 10 wt % or alginate was added to cement in the form of microbeads and solid particles [18, 19]. The alginate microbeads helped the formation of macrochannels in the CPC and biodegradation of material [20]. Other authors [18] reported enhancement of ACP-DCPD compressive strength with the addition of 0.2 and 0.4 wt % sodium alginate ($p < 0.05$). With the further addition of sodium alginate, the compressive strength of the cement declined. The mechanism may involve the inhibition of diffusion of calcium and phosphate ions provided from the dissolution of ACP and DCPD.

The compressive and tensile strengths of the alginate/CPC based on α-TCP were greatly improved after soaking in medium and the formation of apatite crystalline phase was induced when immersed in simulated body fluid [21].

The aim of this study was to investigate the effect of the addition of two different types of sodium alginate (differing in viscosity) on properties of tetracalcium phosphate/nanomonetite (TTCPMH) cement mixture. The setting characteristics, phase composition, microstructure, compressive strength and in vitro cytotoxicity of composite extracts were evaluated.

MATERIALS AND METHODS

Preparation of cement mixtures with the addition of alginate

Tetracalcium phosphate ($Ca_4(PO_4)_2O$, TTCP) was prepared by annealing an equimolar mixture of calcium carbonate ($CaCO_3$, analytical grade, Sigma-Aldrich) and dicalcium phosphate anhydrous (DCPA) ($CaHPO_4$ (Ph.Eur.), Fluka) at 1450°C for 5h. The product was milled in a planetary ball mill (Fritch, 730 rpm) for 2 h and the phase purity was determined using the X-ray powder diffraction analysis (XRD, Philips X Pert Pro, CuKα). The TTCPMH was synthesized by in situ reaction between TTCP and diluted solution (1:4) of orthophosphoric acid (86%, analytical grade, Merck) in ethanol (96%). The H_3PO_4 was added at such amounts that the final Ca/P mole ratio in powder mixtures

equal to 1.67, which corresponds to the Ca/P mole ratio in stoichiometric hydroxyapatite. The sodium alginate/TTCP/nanomonetite composite system was prepared by mixing TTCPMH powder mixture with hardening liquid containing 2% NaH_2PO_4 (analytical grade, Sigma-Aldrich) and sodium alginate. The final content of sodium alginate in composites was 0.25; 0.50; 1.0; 2.0 wt % and 0.25, 0.5 wt % for low (LOW) (Alginic acid sodium salt from brown algae, BioReagent, plant cell culture tested, low viscosity, Sigma-Aldrich) and medium (MED) (Alginic acid sodium salt from brown algae, medium viscosity, Sigma-Aldrich) viscous sodium alginate respectively. The P/L ratio equals 2 for all biocements.

Mechanical testing and characterization methods

The cement paste was molded into pellets (6 mm D x 12 mm H) in stainless cylindrical molds and unaxially pressed at 6 MPa. After setting in 100% humidity at 37°C for 10 min, samples were hardened in 0.9% NaCl solution at 37°C for up to 7 days and, dried at 80°C for 2 hours. The compressive strength (mean of 5 samples) of samples was measured on a universal testing machine (LR5K Plus, Lloyd Instruments Ltd.) at crosshead speeds of 1 mm/min. The statistical evaluation of results (n = 5) was performed using ANOVA analysis at level $\alpha = 0.05$.

The phase compositions of 1 and 7 days hardened samples in 0.9% NaCl solution were analyzed by X-ray diffraction analysis (Philips X´ PertPro, using CuKα radiation) and Fourier transform infrared spectroscopy (FTIR) (Shimadzu, IRAffinity1, 400 mg KBr + 1 mg sample). The microstructures of fractured surfaces of samples were observed by field emission scanning electron microscopy (MIRA3 TESCAN). Relative densities of the samples were calculated from their masses and dimensions. The true density of powder composites was measured by the pycnometer according to EN ISO 3838. The setting times of cement pastes were evaluated according to ISO standard 1566 (Vicat method).

The concentrations of released calcium and phosphate ions after soaking (3 pellets/ 45 ml) of composites in 0.9% NaCl solution at 37°C for 7 days in a closed 50 ml polypropylene tube under dynamic conditions (MINIRotator, 6 rpm) were determined using ICP.

Swelling of alginates was determined from mass differences between origin dry alginate (drying at 100°C) and gel mass after soaking in 0.01 M $CaCl_2$. $2H_2O$ with P/L ratio equal to 1g alginate/200 mL solution. The 150 mg of alginate was uniaxially pressed (50 MPa) into pellet forms (6 mm in diameter) and immersed into Ca^{2+} solution at 25°C for 24 hours. The masses of gels were measured after filtration. Note that solution with Ca^{2+} ions was selected to mimic conditions during cement pastes preparation and setting process.

The amount of carboxylic groups in individual alginate type was evaluated after 24 hours of soaking powders in 0.01M solution of Ca^{2+} ions ($CaCl_2$ solution) at 25°C (pH was adjusted with NaOH solution to 7.4). The content of carboxylic groups in alginates was calculated from the amount of bonded Ca^{2+} ions into precipitates of calcium alginate. Precipitates were filtered and the concentration of calcium ions in supernatants was determined by ICP (Horiba Scientific/Activa optical emission spectrometer).

Cell cultivation and viability testing

Alginate/cement pastes were prepared by mixing powder calcium phosphate mixture with 2% NaH_2PO_4 alginate solution, immediatelly transfered to the form of cylinder shape and composite discs (Ø 7 mm, 1 mm height) were formed. After hardening in 100% humidity at 37°C for 20 minutes, the discs were sterilized in an autoclave at 121°C.

Samples were immersed separatelly into a sterile 50 ml polypropylene tube with complete culture medium composed from EMEM (Eagle´s Minimum Essential medium, Sigma), 10% FBS (fetal bovine serum, Biowest, France) and 1% ATB-ATM (antibiotic-antimycotic solution, Sigma) in a extraction ratio of 3 cm2/ml (according to EN ISO 10993-12:2012). The sample extracts were collected after 24 hours soaking at 37 ºC (incubator, Memmert), centrifuged (5000 RPM/5 min, centrifuge Hettich) to remove possible floating particles and the supernatant was used for cytotoxicity testing.

The cells of mouse preosteoblastic cell line MC3T3E1 (Sigma) were enzymatically released (0.25 % trypsin-EDTA; Sigma) after reaching subconfluence in culture flasks (SPLLife Sciences, Korea), counted (Neubauer hemacytometer) and the cell concentration was adjusted to 1.0x105 cells/ml. Into each well of a 96 well culture plate (Sarstedt, Germany), the 1.0x104 cells in 100 µl of culture medium carrefully were added and incubated at 37°C, 5% CO_2 and 95 % humidity for 24 hours. After 24 hours, the medium from the wells was discarded and exchanged for extracts. The cells in wells were cultivated for 24 hours. As a negative, controls were considered wells with cells cultivated in complete culture medium. After culture, the extracts were exchanged for fresh culture medium with Cell titer aqueus one solution cell proliferation assay (Promega, USA) and the formazan absorbance (produced by viable cells), were measured at 490 nm (Shimadzu UV1800).

RESULTS

XRD and FTIR analysis of cements and composites

The XRD analysis of TTCPMH and alginate composites verified the formation of calcium deficient hydroxyapatite CDHAP (JCPDS 24-0033) after 1 and 7 days of soaking in 0.9% NaCl solution (Fig.1). No differences between the XRD patterns of composites after 1 and 7 days of soaking were found.

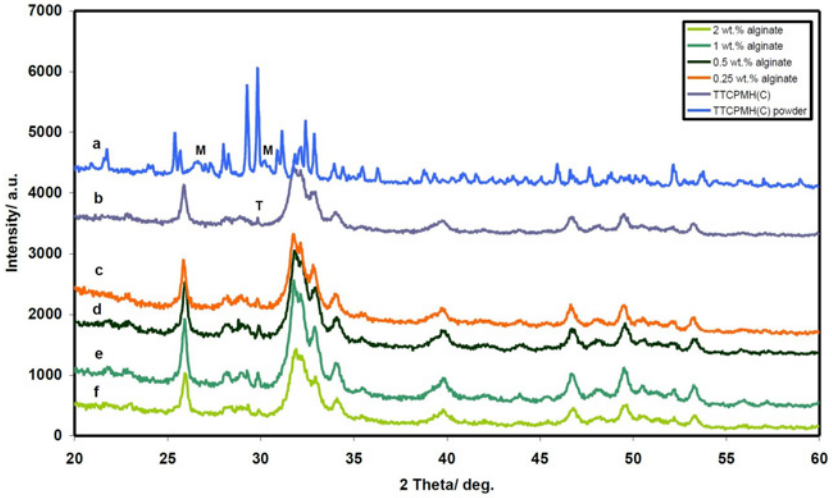

Fig.1. XRD patterns of cements and composites after hardening during 7 days in 0.9% NaCl: a) original TTCPMH powder, b) TTCPMH, c) 0.25 LOW, d) 0.50 LOW, e) 1 LOW, f) 2 LOW.

The FTIR spectra of composites with 0.5 and 2 wt % addition of alginic acid sodium salt (0.5LOW, 0.5MED and 2LOW) after 1 and 7 days hardening in 0.9% NaCl solution are shown in Fig. 2. Characteristic vibrations of the PO_4^{3-} groups in hydroxyapatite arise from antisymmetric (ν_3) and symmetric (ν_1) P-O stretching vibrations located at 1090, 1032 and 962 cm^{-1}, O-P-O bending (ν_4) vibrations at 565 and 602 cm^{-1}, and the librational mode of OH hydroxyapatite group at about 634 cm^{-1} were identified in spectra [22, 23]. Low intense peaks corresponding to ν_3 and ν_2 vibrations of CO_3^{2-} groups at 1479, 1425 and 874 cm^{-1} represent the AB-type of carbonated hydroxyapatite with simultaneously CO_3^{2-} substitution for PO_4^{3-} and OH^- groups [24]. The peak from stretching vibrations of the OH hydroxyapatite group was observed at 3560 cm^{-1}. Note that no additonal bands from vibrations of alginate were revealed in spectra probably due to the low intensity of vibrations of polysaccharide groups and lower alginate content in composites.

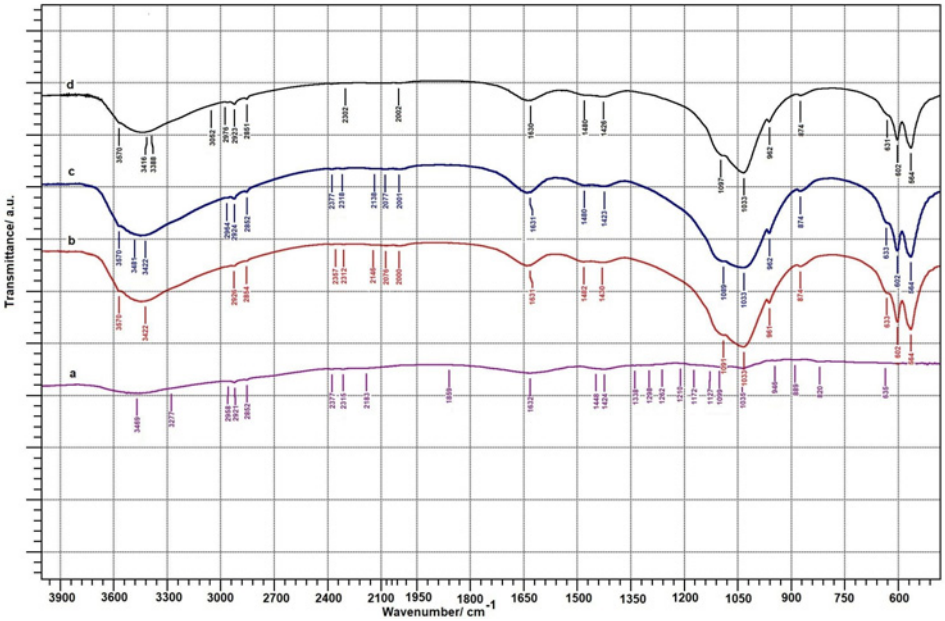

Fig.2. FTIR spectra of composites with 0.5 wt % and 2 wt % addition of sodium alginate after 1 day hardening in 0.9% NaCl: a) prepared calcium alginate, b) 0.5 LOW, c) 0.5 MED, d) 2 LOW.

Microstructure of hardened composites

The microstructure of fractured cements with 0.5 wt % and 2 wt % of sodium alginate salt after 1 day of hardening in 0.9% NaCl is shown in Fig. 3.

The coarse agglomerates of fine thin plate-like particles (size up to 500 nm) and cement matrix composed of globular particles were visible in the microstructure of pure cement. A high density of irregularly shaped micropores with size up to 2 μm and a small volume fraction of larger around 10 μm pores were observed in the microstructure. Fine thin needle-like nanohydroxyapatite particles with length up to 1 μm are arranged into the form of 5–10 μm agglomerates.

From a macroscopic point of view, the microstructures of all composite cements are very similar. A high number of larger irregularly shaped 2-10 μm micropores can be visible in microstructures. In LOW composites containing less than 2 wt % alginate the spherical particle agglomerates composed of fine needle-like hydroxyapatite particles with length does not exceed 100 nm. Note that individual agglomerates were not mutually tightly interconnected across boundaries via nanohydroxyapatite particles and agglomerates were separated from each other. In the case of cements with higher alginate content (LOW) and 0.5MED cements, a significantly lower amount of needle-like particles was created during the cement transformation and the granular fine nanoparticles connected to form irregularly shaped agglomerates of 5-10 μm size can be visible in microstructures.

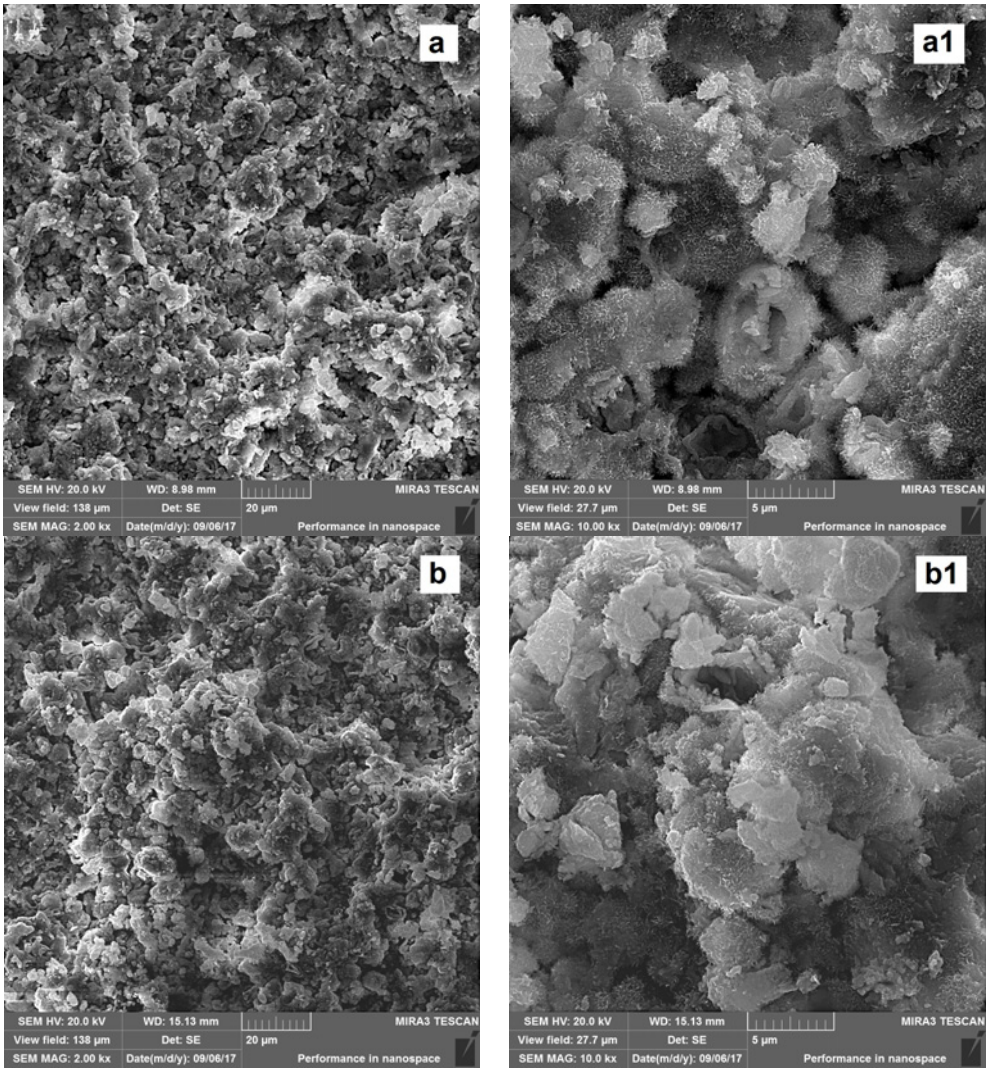

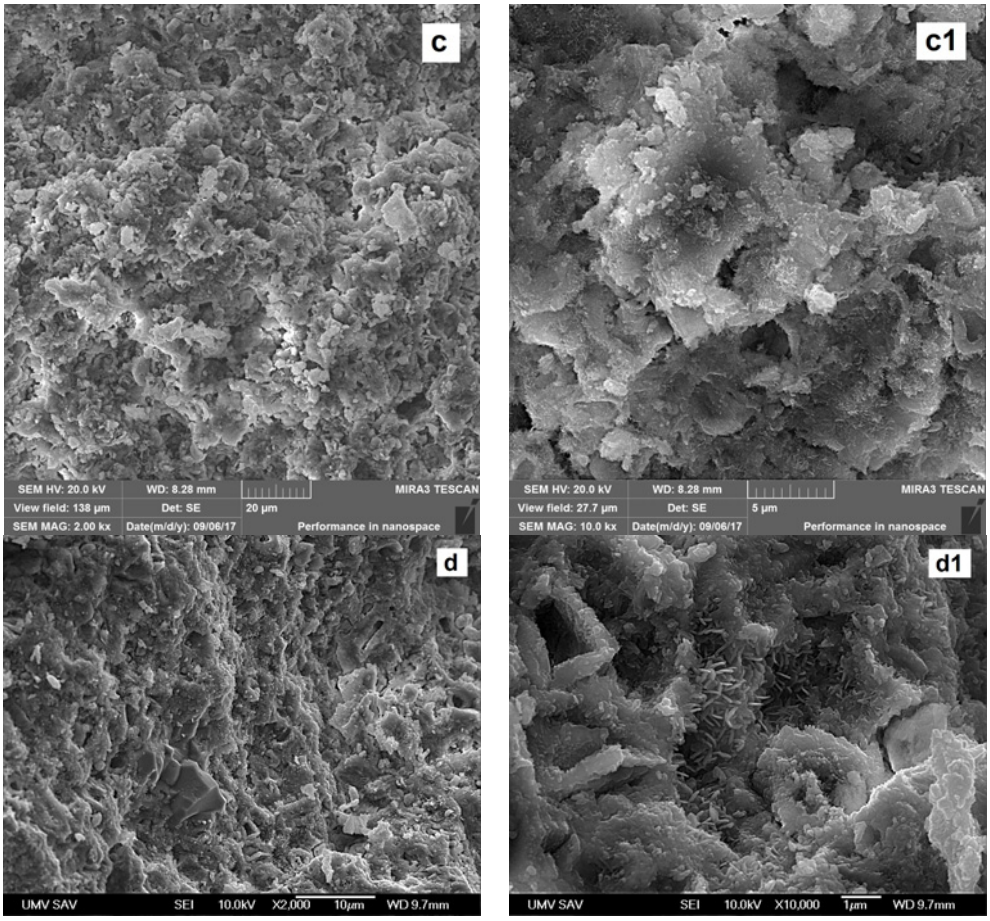

Fig.3. Microstructure of fractured cements with 0.5 wt % and 2 wt % of sodium alginate salt after 1 day of hardening in 0,9% NaCl: (a, a1) 0.5 LOW, (b, b1) 0.5 MED, (c, c1) 2 LOW, (d, d1) TTCPMH.

Cytotoxicity of extracts and evaluation of physico-chemical characteristics of alginates and powder composites

From cytotoxicity testing it resulted that the relative proliferations of osteoblasts cultured in sample extracts were not statistically different ($p>0.65$) and had a low cytotoxicity potential (no statistical difference from 70 % level for cell viability represents limits of the potential cytotoxicity of the sample (STN ISO 10993-5). The concentrations of calcium and phosphate ions released from 0.5 wt % alginate cement powder mixtures to 0.9% NaCl solution at 37°C and dynamic experimental conditions were evaluated after 2 and 24 hours of soaking (Table 1).

Relative standard deviations for determination of Ca^{2+} and PO_4^{3-} concentrations were 5% and 7% respectively.

Tab.1. Concentrations of Ca^{2+}, PO_4^{3-} ions after soaking of composites samples in 0,9% NaCl solution at 37°C for 2 and 24 hours.

Sample	Ca^{2+}/mM		PO_4^{3-}/mM	
	2h	24h	2h	24h
C + 0.5 wt % Alg. low	1.40	0.42	5.21	<0.05
C + 0.5 wt % Alg. med	1.43	0.76	0.49	<0.05

Results showed the rise in concentrations of both ions in solution after 2 h soaking with the following about 50% decrease in Ca^{2+} whereas the concentration of phosphate ions was very low irregardless of alginate type after 24 h soaking. An almost ten times higher concentration of phosphate ions was found in LOW than MED cement suspensions after 2 h soaking. The significant differences were revealed in swelling alginate cements where an about 56-fold rise in mass of MED alginate was found contrary to the 35-fold rise of LOW alginate after swelling. Similarly the MED and LOW alginates contained various amounts of carboxylates per gram, thus, 0.494±10 and 0.362±9 mmol carboxylates/1 g alginate respectively.

Compressive strength and setting time of composites

Results of the analysis of stress/strain curves are shown in Fig.4. The comparison of curves verifies the same character of dependence with a strong reduction of both parameters (around 70% and 30 % decrease in the work of fracture (WOF) and Young´s modulus respectively) after 0.25 wt % addition of low alginate. Statistically significant difference in the work of fracture was found between of 0.25 and 0.5 lowALG biocements ($p<0.035$) whereas no statistical differences were revealed between WOF of 0.5 and 1 lowALG biocements ($p>0.357$).

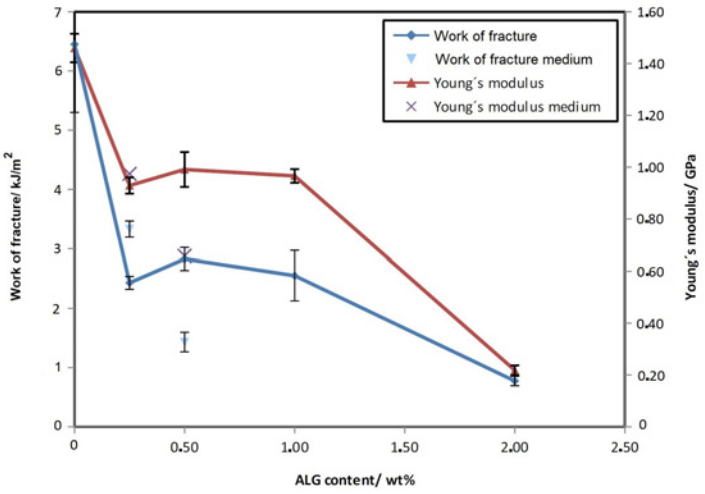

Fig.4. Dependence work of fracture and Young´s modulus on alginate content (wt %).

In the case of Young´s modulus, no statistical differences were identified between 0.25 and 0.5 ($p>0.221$) as well as 0.5 and 1 ($p>0.581$) lowALG biocements. Both the Young´s modulus and WOF of medALG samples significantly decreased after the addition of 0.25 and 0.5 alginate ($p>0.6$). Note that the rise in alginate content to 2 wt% caused rapid

decrease in WOF and Young´s modulus of LOW biocement. Very similar dependences of CS on content or alginate viscosities can be observed in Fig.5 which clearly demonstrate about a 50 % reduction of CS in 0.25 or 0.5 and 1 LOW biocements with a further approx. 50% reduction in 2 LOW cement.

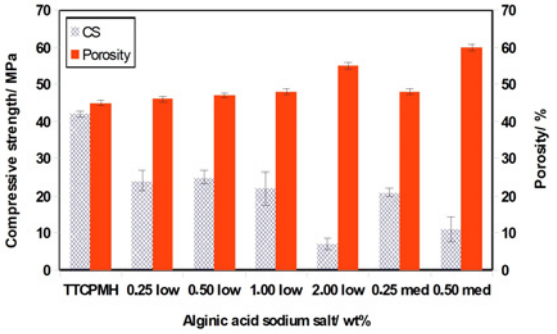

Fig.5. Effect of compressive strength and porosity of cements on addition of sodium alginate.

After 7 days of hardening, the porosities of LOW composites (up to 1 wt % of alginate) and 0.25 MED composite were around 47±1% of true density, which was almost the same as the porosity of pure cement (46±2%), and decreased in 2 LOW and 0.5 MED composites to 55±2 and 60±2% respectively.

The setting time of 0.5MED composite cements was 14 min contrary to 5 min of 0.5LOW and TTCPMH cements. Note that setting times of all LOW cement mixtures were close to 5 min.

DISCUSSION

Two types of alginates with different viscosity of gels were studied as additives in calcium phosphate biocement. The small addition of MED alginate (higher viscosity) caused strong changes (reduction) in mechanical properties, setting time and suppress workability of cement paste. On the other hand, a similar about 50% decrease in mechanical properties (CS, Young´s modulus, WOF) was revealed after an addition of 0.25 wt % of LOW alginate with their rapid fall above 1 wt % content of LOW alginate in biocement. It is known that dependence of mechanical properties on density of cements and the fast reduction of composite cement strength at higher contents of alginates could be related to an increase in cement porosity. Apart from this, enhanced amounts of granular or finer needle-like nanohydroxyapatite particles arranged to form of more separated spherical agglomerates were observed in microstructures of composite cement contrary to the large fraction of agglomerates composed of longer needle-like particles in the more compact microstructure of TTCPMH cement. The mentioned effects clearly show strengthening in its microstructure across boundary of agglomerates via nanohydroxyapatite particles whereas weak boundary strengthening can be only assumed in the case of composites. The large stresses are induced in microstructure after drying of cements due to contraction of swelled alginates which significantly helps to debond and aid separation of particle agglomerates in cement composites. Note that a similar decrease in mechanical properties was also measured in wet composite cements but the presence of gels in microstructures clearly enhanced creep with a reduction of friction between individual agglomerates.

About a 30% higher content of carboxylates in MED than LOW alginates may seem in contradiction with the above results because a higher amount of carboxylic groups indeed bound more calcium ions released during hydrolysis and transformation of cement components. It follows the possible strengthening structure via alginate chains, but the fast rise of setting time with MED alginate content in cements as well as the higher concentration of phosphate ions in the initial stage of setting verified inhibition of the cement transformation process. Also demonstrated was the nucleation of an enhanced number of hydroxyapatite nuclei with following refinement of final nanohydroxyapatite particles in microstructure due to the presence of a larger amount of calcium ions trapped on alginate chains. Despite the initial inhibition of setting process in composites, the full transformation of starting calcium phosphate phases was demonstrated after 24 hours hardening. Note that the LOW alginate amount (up to 2 wt %) only slightly affected by setting time of cement composites. It may be speculated that LOW alginate was more susceptable to degradation during soaking in NaCl solution, but analysis of the carbon content in cements revealed no changes in the carbon contents between freshly prepared composites and samples 7 days hardened.

It was shown that the addition of alginate to CPC or ACP-DCPD resulted in an increase of setting time [16]. The organic compounds with the charged functional groups (OH^-, NH_2^-, COO^-) had a great effect on the hydration reaction of calcium phosphates. Generally, the final setting times of cements with organic compounds were all increased but sodium alginate had the largest influence [17]. The other authors [6] reported that sodium alginate inhibits the CPC conversion to HAP during setting reaction. A strong decrease in the flexural strength from 8.4±1.8 MPa to 2.3±0.4 MPa was found in TTCP/DCPA cement and composite containing 50% microbeads respectively [19]. The mechanical strength (diametral tensile strength) of the cement (TTCP/DCPA) increased rapidly with the addition of sodium alginate up to 0.8 wt % (around 6 MPa) and soaking in distilled water at 37°C. The further addition of sodium alginate (SA) caused a decrease the mechanical strength and inhibition of the setting reaction. Setting time of our TTCPMH cements with LOW alginate was close to this one in non decayed fast setting TTCP/DCPA cement mixture which contained submicron particles of DCPA [25]. However, the content of origin TTCP phase was lower than in the above mixture, which verifies the faster transformation process of more active nanomonetite particles. In the case of α-TCP based cement, the initial hardened cement had a compressive strength of ~10 MPa and the value increased significantly up to ~60-70 MPa after 3-7 days of incubation in SBF [21]. It is clear from the above facts that generally an addition of alginate to composites mainly reduced mechanical properties of cements, but probably this change depends on the type of calcium phosphate cements. Note that the effect of different alginate viscosity on properties of alginate/CPC composites were not studied in literature, and it is hard to compare our results with other papers.

CONCLUSIONS

The small addition of two alginate types reduced compressive strength of TTCPMH cement. A gearter inhibition effect of MED alginate (more viscous, higher amount of carboxylic groups and stronger swelling) on setting process and the decrease in CS of composites was found, which demonstrates favorable properties of LOW alginate for utilization as the additive in TTCPMH cement. On the other hand, the prolongation of setting time at low content of MED alginate may be considered as a positive property in application of composite as the injectable cement paste, but the higher viscosity of composite paste significantly impairs its workability.

Acknowledgement

This work was supported by the Slovak Grant Agency of the Ministry of Education of the Slovak Republic and the Slovak Academy of Sciences, Project APVV-17-0110.

REFERENCES

[1] Khairoun, I., Driessens, FCM., Boltong, MG., Planel,l JA., Wenz, R.: Biomaterials, vol. 20, 1999, p. 393
[2] Krebs, J., Aebli, N., Goss, BG., Sugiyama, S., Bardyn, T., Boecken, I., Leamy, PJ., Ferquson, SJ.: J. Biomed. Mater. Res. B Appl. Biomater., vol. 82, 2007, p. 526
[3] Calo, E., Khutoryanskiy, VV.: Eur. Polym. J., vol. 65, 2015, p. 252
[4] Olderøy, MO., Xie, M., Andreassen, JP., Strand, BL., Zhang, Z., Sikorski, P.: J. Mater.Sci.:Mater. Med., vol. 23, 2012, p. 1619
[5] Perez, RA., Kim, HW., Ginebra, MP.: J. Tissue Eng., vol. 3, 2012, 2041731412439555
[6] Ishikawa, K., Miyamoto, Y., Takechi, M., Toh, T., Kon, M., Nagayama, M., Asaoka, K.: J. Biomed. Mater. Res., vol. 36, 1997, p. 393
[7] An, J., Wolke, JGC., Jansen, JA., Leeuwenburgh, SCG.: J Mater. Sci: Mater. Med., vol. 27, 2016, p. 58
[8] Hempel, U., Reinstorf, A., Poppe, M., Fischer, U., Gelinsky, M., Pompe, W., Wenzel, K.W.: J. Biomed. Mater. Res. B, vol. 71, 2004, p. 130
[9] Miyamoto, Y., Ishikawa, K., Takechi, M., Toh, T., Yuasa, T., Nagayama, M., Suzuki, K.: Biomaterials, vol. 19, 1998, p. 707
[10] Miyazaki, K., Horibe, T., Antonucci, J.M., Takagi, S., Chow, LC.: Dent. Mater. vol. 9, 1993, p. 41
[11] Mickiewicz, RA., Mayes, AM., Knaack, D.: J. Biomed. Mater. Res., vol. 61, 2002, p. 581
[12] Cherng, A., Takagi, S., Chow, LC.: J. Biomed. Mater. Res., vol. 35, 1997, p. 273
[13] Fujishiro, Y., Takahashi, K., Saito, T.: J. Biomed. Mater. Res., vol. 54, 2001, 525
[14] Xu, HHK., Simon, CG.: Biomaterials, vol. 26, 2005, p. 1337
[15] Xu, HHK., Quinn, JB., Takagi, S., Chow, LC.: Biomaterials, vol. 25, 2004, p. 1029
[16] Chen, CHD., Chen, CC., Shie, MY., Huang, CH., Ding, SJ.: Mater. Sci. Eng. C, vol. 31, 2011, p. 334
[17] Yu, T., Ye, J., Gao, C., Yu, L., Wang, Y.: Colloids Surf. B Biointerfaces, vol. 75, 2010, p. 363
[18] Wang, X., Chen, L., Xiang, H., Ye, J.: J. Biomed. Mater. Res. B vol. 81, 2007, p. 410
[19] Zhou, H., Weir, MD., Xu, HH.: Tissue Eng. Part A, vol. 217, 2011, p. 2603
[20] Lian, Q., Li, DC., He, JK., Wang, Z.: Proc. Inst. Mech. Eng. H, vol. 222, 2008, p. 347
[21] Lee, GS., Park, JH., Won, JE., Shin, US., Kim, HW.: J. Mater. Sci: Mater. Med., vol. 22, 2011, p. 1257
[22] Bohner, M.: Injury, vol. 31, 2000, p. 37
[23] Krajewski, A., Mazzocchi, M., Buldini, PL., Ravaglioli, A., Tinti, A., Taddei, P., Fagnano, C.: J. Mol. Struct., vol. 744-747, 2005, p. 221
[24] Apfelbaum, F., Diab, H., Mayer, I., Featherstone, JDB: J. Inorg. Biochem., vol. 45, 1992, p. 277
[25] Ishikawa, K., Miyamoto, Y., Kon, M., Nagayama, M., Asaoka, K.: Biomaterials, vol. 16, 1995, p. 527

sciendo Powder Metallurgy Progress, Vol.19 (2019), No.1, p.012-022
http://dx.doi.org/10.1515/pmp-2019-0002

STUDY ON SINTERING OF ARTIFICIALLY OXIDIZED STEEL COMPACTS

C. Gierl-Mayer, T. Stepan, J. Sun, H. Danninger

Abstract

Sintering of Cr-prealloyed PM steels requires atmospheres with good quality – low oxygen potential – to achieve satisfactory sintering results. But during heating even the best atmospheres may be oxidizing, the system turns to reducing conditions only at high temperatures, which can be monitored by thermal analysis. During the dewaxing process, oxidizing conditions are favourable for effective dewaxing without sooting and blistering. However, this may result in some oxygen pickup during heating, and then the final properties of the produced parts may be strongly influenced by this intermediate oxidation. This study demonstrates the behaviour of artificially oxidized steels (Fe-C and Fe3Cr-0.5Mo-C) during the sintering process by stepwise sintering. Iron and steel powder were slightly oxidized and then pressed and sintered at different temperatures. In parallel, as a second approach, pressed samples were oxidized and then sintered. Density, hardness and impact energy were measured and dilatometry/MS was used for online monitoring of the sintering process. The starting oxygen content of 0.20 to 0.30 wt% is high enough to change the sintering behaviour of the materials, but still leads to rather good properties. Thermal analysis showed that most of the oxygen picked up was present as iron oxides on the surface which were reduced by hydrogen at rather low temperatures, confirming that these were iron oxides, which also holds for the Cr-prealloyed variant. The biggest influence on the final performance was exerted by the final carbon content and the microstructural development of the material.

Keywords: sintering behaviour, mechanical properties, oxygen, "Oxidation" reduction, decarburization

INTRODUCTION

Sintering of Cr-prealloyed PM steels opens new markets in terms of interesting mechanical properties for PM parts, but since chromium is more oxygen sensitive than iron, the requirements for sintering of these materials have changed compared to classical PM steels. In [1-4] it is demonstrated that Cr prealloyed powders contain an Fe oxides layer on their surface with disperse particulates of complex oxides. Consequently the sintering requires deoxidation at low temperatures by hydrogen to prevent "internal gettering", i.e. oxygen transfer from iron oxides on the surface to the more stable elements [5]. This oxygen transfer should be avoided since once these more stable oxides are formed, higher sintering temperatures are required for reduction, which means that the mechanism is carbothermal reduction.

Christian Gierl-Mayer, Thomas Stepan, Jie Sun, Herbert Danninger: Institute of Chemical Technologies and Analytics, TU Wien. Vienna, Austria.

The discussion whether it is direct or indirect reduction is still ongoing [6]. The carbothermal reduction influences the final carbon content of the sintered material and therefore the mechanical properties and the dimensional behaviour. But even when the best sintering conditions are applied the dewaxing process has to be kept in mind. Usually the dewaxing is more effective in slightly oxidizing atmospheres to break down the long-chain additives effectively in order to avoid sooting and blistering. However, this treatment may result in oxygen pickup during the initial stages of the sintering run.

In this article it is tried to identify the effects of such intermediate oxidation. It describes the influence of an artificial oxidation on the final properties by stepwise sintering and dilatometric experiments to identify the critical temperature ranges and the sintering mechanisms.

EXPERIMENTAL PROCEDURE

Plain iron (ASC100.29) and prealloyed Fe-3Cr-0.5Mo (AstaloyCtM) – both from Höganäs AB - were chosen as test materials. The final mixture was Fe-0.5C and Fe3Cr-0.5Mo-0.5C whereas carbon was added as graphite (Kropfmühl UF4). The experiments of this study were performed in two steps. The first step was to find conditions for reasonable, but not too pronounced, oxidation of the powder, so 300° and 400°C for 30 and 60 min were chosen, in all cases in air. For oxidation at 300°C a drying chamber was used, and for 400°C a tube furnace was purged with air.

The oxidation was performed in two different ways: The first variant was to oxidize the pressed samples, compacted at 600 MPa in a floating die (55x10x10 mm^3, charpy bars according to ISO 5754) with die wall lubrication. This method should demonstrate the effects of oxidation which might occur during the debinding or sintering process if the atmosphere is not adequate at low temperatures. The second variant was to oxidize the base ferrous powder (before mixing with graphite) in a steel boat placed in a drying chamber. This variant was chosen to prove the effect of freshly reduced surfaces which are said to be more active in sintering than the standard powder. Originally the oxidation of the powder was planned for 400°C, too, but analysis of pressed samples showed that oxidation was too severe at 400°C, so this experiment was skipped (see also LOM and SEM pictures of the broken surfaces in Fig. 1 and 2).

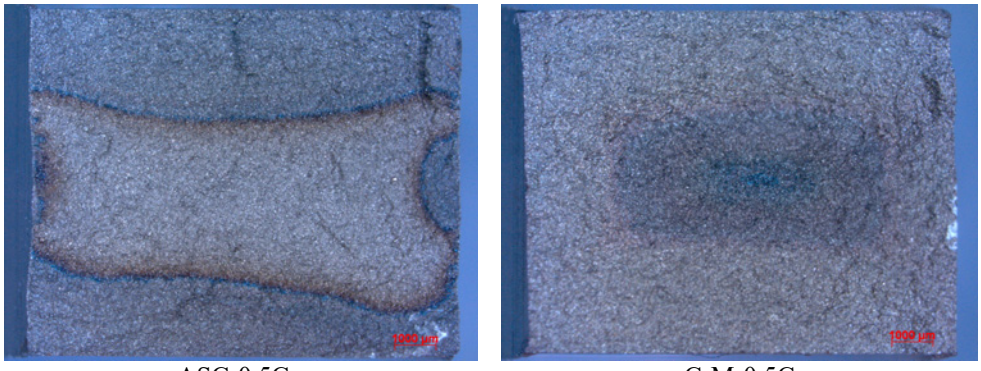

ASC-0.5C CrM-0.5C

Fig.1. Fracture surfaces of samples after oxidizing treatment at 400°C for 60 min in air; macroscopic images.

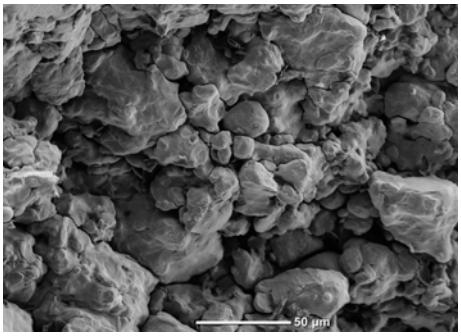

a) Fe-0.5C untreated

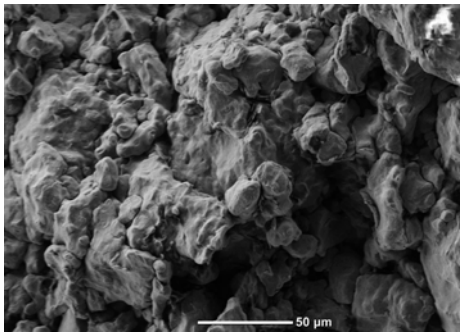

b) Fe-0.5C 400°C 60 min

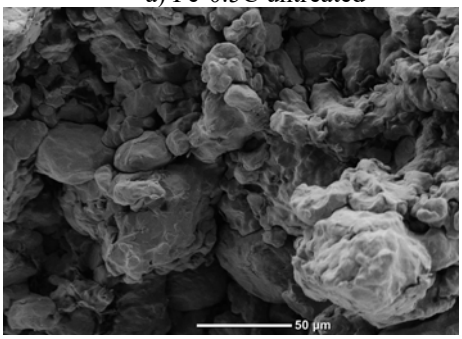

c) Fe-3Cr-0.5Mo-0.5C untreated

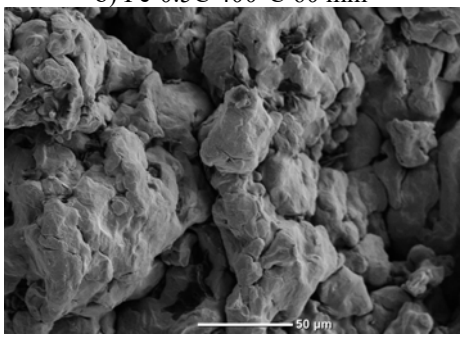

d) Fe-3Cr-0.5Mo-0.5C 60 min 400°C

Fig.2. Fracture surfaces untreated and after oxidation at 400°C; SEM images.

Tab.1. Oxygen analysis of initial trials

sample	treatment	Oxygen [wt%]	± [wt%]
Powder: ASC100.29	as delivered	0.094	0.002
	30 min 300° air	0.222	0.008
	60 min 300° air	0.261	0.009
Powder: AstaloyCrM	as delivered	0.187	0.007
	30 min 300° air	0.264	0.002
	60 min 300° air	0.280	0.008
ASC+0.5C 600MPa	untreated	0.172	0.014
	30 min 300° air	0.215	0.025
	60 min 300° air	0.245	0.023
	30 min 400° air	0.251	0.047
	60 min 400° air	0.519	0.018
CrM+0.5C 600 MPa	untreated	0.146	0.008
	30 min 300° air	0.296	0.044
	60 min 300° air	0.290	0.007
	30 min 400° air	0.388	0.072
	60 min 400° air	0.499	0.086

Table 1 shows the oxygen analysis for these initial trials. It is easy to see that oxidation at 400°C is too severe, thus 300°C for 60 min in the drying chamber was the temperature chosen for the main experiments. As a reference, untreated powder was

pressed, and the specimens were characterized. Compared to the usual O-contents of the used powders (typically 0.08 wt% for ASC 100.29 and 0.16 wt% for AstaloyCrM) the effect of the oxidation is evident. The untreated ASC-sample showed improbable, high oxygen contents, which is obviously caused by the Multical oil used for die wall lubrication. The results show that at 300°C the oxidation seems to reach a stable state at 30 min whereas at 400°C the effect of soaking time is much stronger. As already shown in [7] the Cr-prealloyed material is not very sensitive to oxidation al low temperatures, since the oxygen levels are comparable to those of plain iron powder, although CrM is reported to be a very oxygen-sensitive powder. The oxidation of the pressed samples was inhomogeneous (which was intended) and easily can be seen in Fig. 1. Therefore differences between homogeneous (samples pressed of oxidized powders) and inhomogenous samples (oxidized green compacts) can be investigated.

The main experiments were performed with artificial oxidation at 300°C in air in a drying chamber. To study the sintering behavior, stepwise sintering was performed at 700, 800, 900, 1000, 1100, 1200 and 1250°C in $N_2/10\%H_2$ (5.0 purity) for 30 min in a pusher furnace with gas-tight superalloy tube retort. Additionally, sintering experiments in a dilatometer (Netzsch 402C) coupled with mass spectrometer (MS Netzsch Aeolos, capillary coupling) were performed in pure hydrogen with all 3 sample variants (untreated, artificial oxidized samples and samples fabricated of oxidized powder). Here also full charpy bars were used. The parameters were: 10 K/min heating and cooling, T_{max} 1300°C held for 60 min, recorded masses: 2 (H_2), 12 (C), 14 (N), 15 (CH_3), 16 (CH_2, O), 17 (OH), 18 (H_2O), 28 (N_2, CO), 32 (O_2), 44 (CO_2).

All mechanical physical and mechanical properties were determined by the samples sintered in the furnace experiments.

RESULTS AND DISCUSSION

The average green density of Fe-0.5C was 6.96±0.02 g/cm³ which increased slightly after oxidation treatment to 6.98±0.02 g/cm³. The green density of the oxidized and then compacted powder was 6.95±0.03 g/cm³. The same trend was observed with Fe-3Cr-0.5Mo+0.5C, in which case the reference green density was 6.75±0.02 g/cm³, and after oxidation treatment 6.77±0.02 g/cm³, whereas the green density of the oxidized powder material was 6.70±0.03 g/cm³. This means that the green density is only slightly influenced by the treatment and that the starting point in terms of density changes during sintering is rather the same for all variants - for sure the green density of the prealloyed material is much lower than Fe-0.5C.

The sintered density does not show too pronounced effects of oxidation except for the fact that densification is enhanced especially in the Cr-prealloyed system at high sintering temperatures (Fig. 3). It is well known that the impact energy is a strong indicator for the quality of the sintering process, as indicated by the strength of the sintering contacts. The significant “delay” in the increase of the impact energy with temperature visible for the oxidized Fe-0.5C variants compared with the untreated material – the difference being most pronounced at 800°C - (Fig. 4) is strongly connected to the development of the microstructure which is demonstrated in Fig. 5. Only at 800°C sintering temperature there is a significant difference in the microstructure. Whereas the reference material already shows some sintering contacts and carbon dissolution (appearing as pearlite), the oxidized variants look like more or less like green bodies. From 900°C on this difference tends to disappear, and the oxidized parts reach comparable impact energies as the reference material or even better ones (1250°C). The material produced from the oxidized powder shows a very similar behavior, but does not reach the level of the reference material.

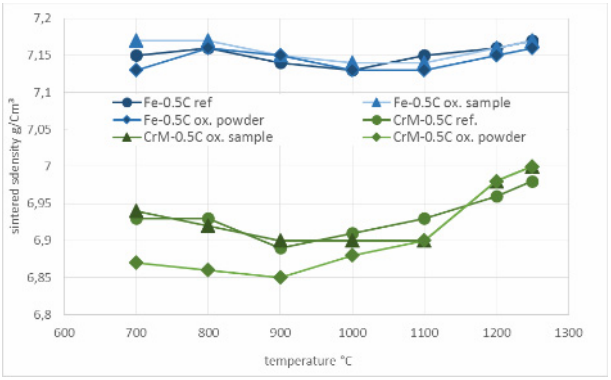

Fig.3. sintered density of differently treated PM-steels sintered 30 min. at varying temperatures in N_2-10%H_2.

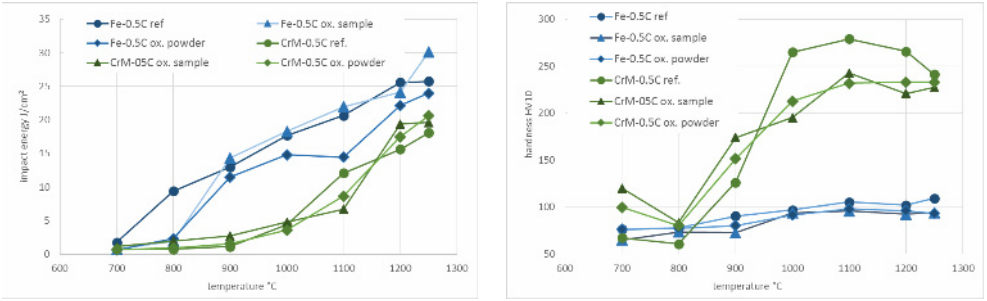

a) b)

Fig.4. Impact energy (a) and hardness (b) of differently treated PM steels. Sintered 30 min. at varying temperatures in N_2-10%H_2

The influence of the oxidation seems to be negligible for the Cr-prealloyed material. Although there are marked differences in microstructure development from 700 to 900°C the difference in impact energy is negligible (see Fig. 4a). For sure the general impact energies reached at these sintering temperatures are rather low, indicating that the sintering contacts have not been developed very well. This holds also for the reference materials and agrees with the findings described in [8]. The microstructure shows another phenomenon: In contrast to Fe-C, in the Cr-prealloyed steels the development of the sintering contacts is not linked to carbon dissolution. It can be easily seen that carbon dissolution is strongly dependent on the starting material. Whereas the reference material shows the first dissolution of carbon at 900°C the oxidized variants show some pearlite already at 800°C, also indicated by a strong increase of hardness, although the impact energy and therefore the sintering contacts are not developed very well. In the micrographs, apart from the carbon dissolution also the presence of an oxide layer on the former powder particles is discernible. For this material much higher temperatures are required – at least above 900°C - to develop the desired microstructures, as can be seen for sintering temperatures of 1100 and 1200°C [8]. This material is a perfect example that hardness by itself is not an indicator for proper sintering, also strength data are required, which means that the ratio of tensile strength to hardness should be in the range of 3.2 as described e.g. by Momeni et al. [10].

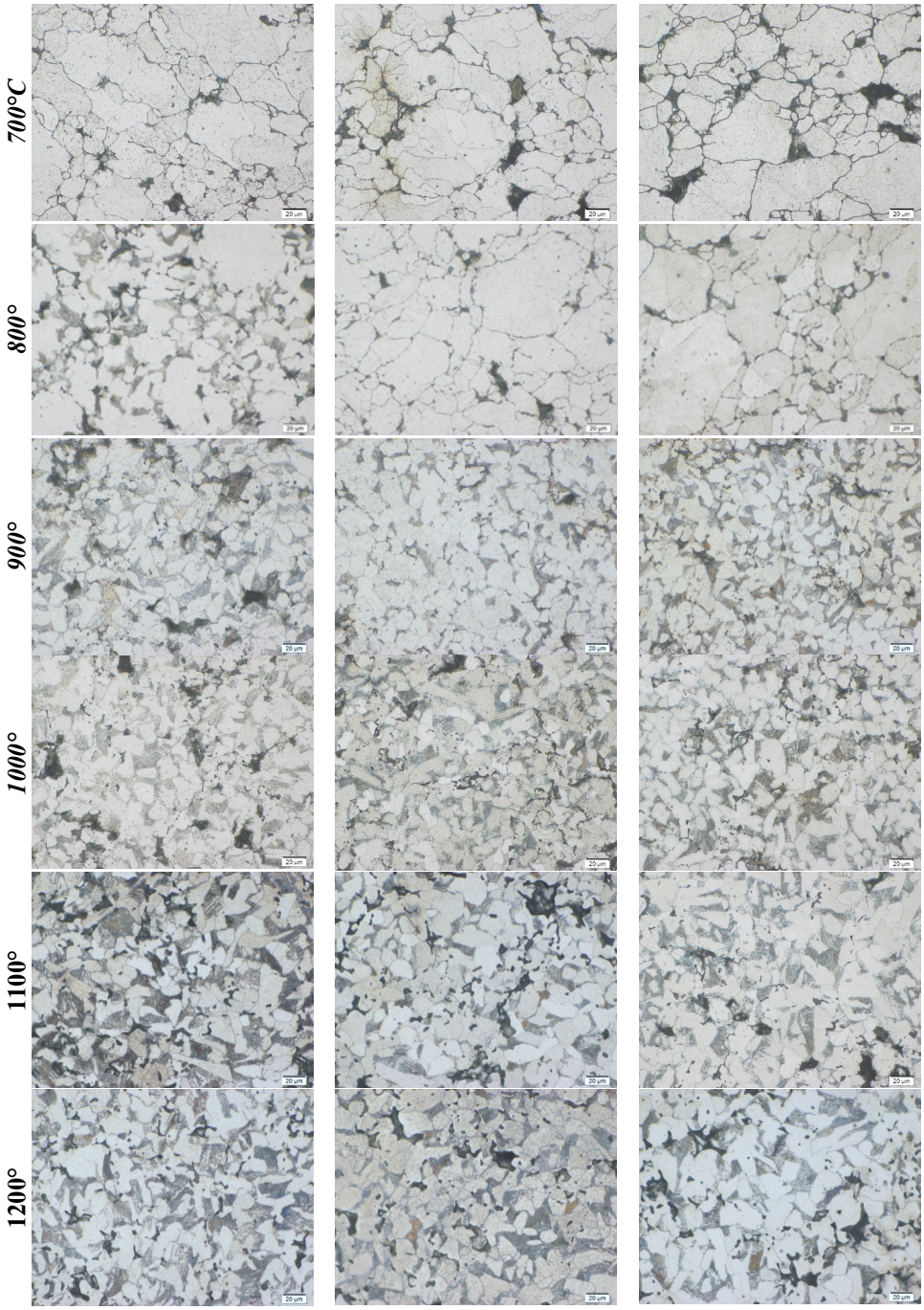

Fig.5. Microstructures of different treated Fe-0.5. Sintered 30 min at 800°-1200° in N_2-10%H_2.

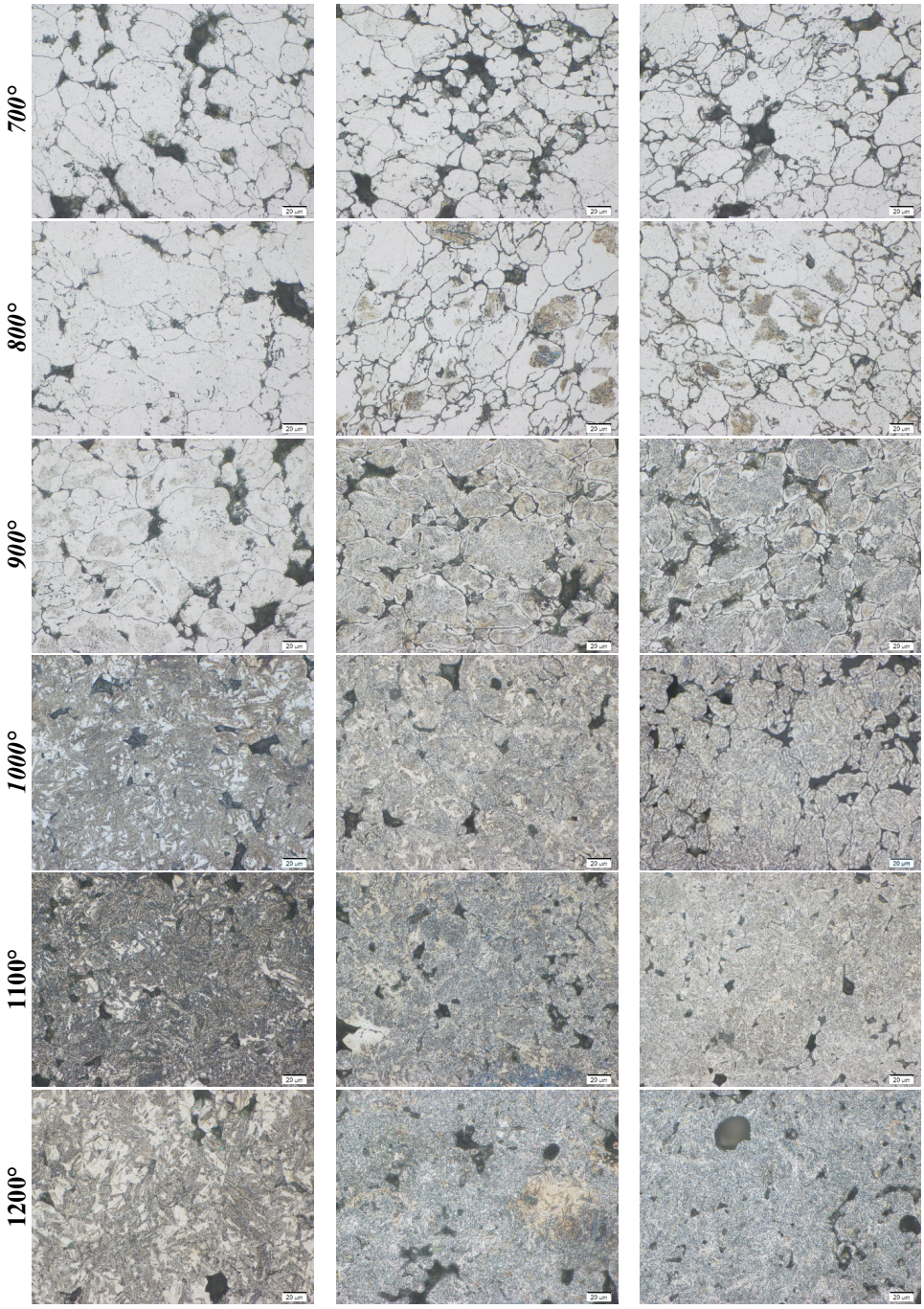

a) reference b) oxidized green body c) oxidized powder

Fig. 6: Microstructures of different treated Fe-3Cr-0.5Mo-0.5C. Sintered 30 min at 800°-1200°C in N_2-10%H_2

When comparing the hardness development of both materials the difference is evident. The system Fe-C shows a more or less linear increase due to pearlite formation and strengthening of the sintering contacts. The Cr-prealloyed material shows much more complex microstructures as already mentioned. Since this material not only transforms to pearlite during cooling but also in part to bainite, the rise in hardness is much stronger. The ratio bainite/pearlite also depends on the overall carbon content which is higher for the reference material at sintering temperatures above 1000°C (see Fig. 6) which then again enhances the transformation to bainite.

The trends for the carbon and oxygen contents of the reference materials are as expected (Fig. 7). The reference material at 700°C shows the carbon originally added to the powder mix. At 1000°C sintering temperature, when significant carbothermal reduction processes occur, the material shows marked carbon loss. The artificially oxidized Fe-0.5C specimens, both from oxidized compact and oxidized powder, differ from the reference at and above 900°C sintering temperature, showing significantly higher carbon loss due to the necessary reduction processes. It is interesting that the reduction of the artificially oxidized samples needs higher temperatures, which can be observed by the carbon loss, as the reduction is obviously done by carbothermal reduction, and final oxygen content of the material fit very well with the expected results derived from dilatometry experiment of these powders. The sensitivity of the material to the oxidizing treatment can be seen from the oxygen content. Only at the highest sintering temperatures, the usual, expected oxygen content and therefore the desired mechanical properties are attained.

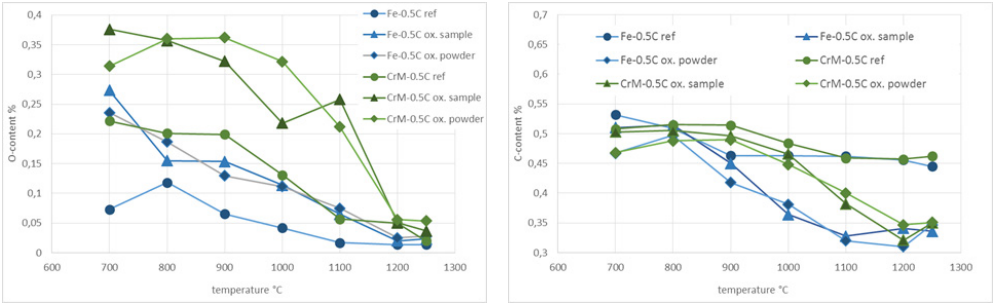

a) carbon content b) oxygen content

Fig.7. Interstitial content of differently treated PM steels. Sintered 30 min. at varying temperatures in N_2-10%H_2.

Monitoring the sintering experiments by dilatometry coupled with mass spectrometry (MS) showed that although the Cr-material is expected to be more sensitive to oxidation, both materials exhibit very similar behaviour when oxidized at rather low temperatures (Fig.8). The artificial oxidizing of Fe-0.5C material indicates that mainly the surface of the material is oxidized which is revealed by the larger peaks of water (m18) in the early (= low temperature) region of the sintering process. When comparing the oxygen content it is clear that even sintering at a temperature of 800°C in N_2-H_2 is sufficient to significantly reduce the oxygen content. The internal oxides are not affected to the same degree, the peaks of m28 are only slightly higher compared to the reference material. This little higher consumption of carbon as reducing agent explains the slight difference in oxygen content and final carbon content in the sintered samples. The difference caused by the heating rates, slow heating in the dilatometer experiment and fast heating in the furnace,

is rather small for the Fe-C system, but there seems also to be a slight “internal getter” effect.

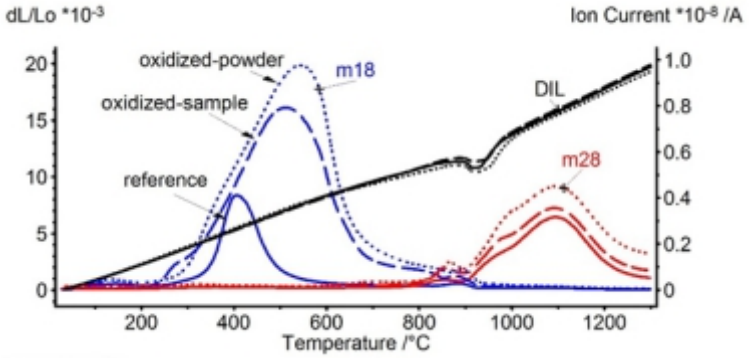

a) Fe+0.5C

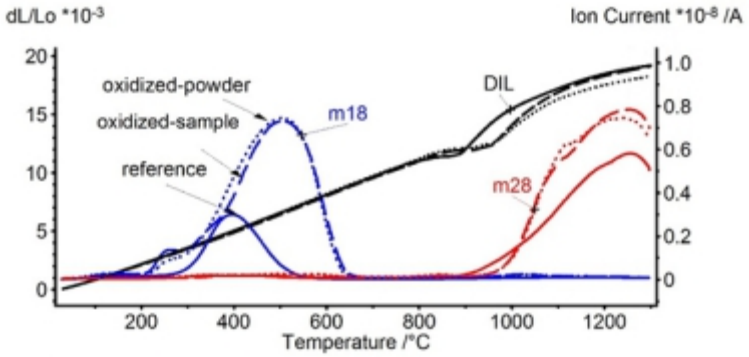

b) Fe-3Cr-0.5Mo+0.5C

Fig.8. DIL-MS vs. temperature of differently treated PM-steels (untreated and oxidized samples, samples produced of oxidized powder, full charpy bars), 10 $Kmin^{-1}$, 60 min 1300°C heating section, plain H_2.

For the Cr-steel it is interesting to see that the strongest increase in deoxidation, i.e. the most pronounced reduction peak, is not observed for the more stable oxides but for the surface oxides indicated as iron oxides by their reducibility in H_2 at low temperatures, which agrees very well with the findings in [7]. Also here the water peak (m18) is much larger compared to the reference material. But here we see significant differences between the pusher furnace experiments and the dilatometer since the heating of the material is done in different ways. Whereas in the dilatometer the samples are heated at constant rate (10 K/min), in the experiments in the furnace the boats with the samples are placed in the hot zone of the furnace and are heated up according more or less to the heat capacity of the material. When heated in the furnace, low temperature reduction by H_2 is only very limited, and the oxygen transfer of the surface oxides to more stable ones (“internal gettering”) can occur whereas this will not happen in the dilatometer since the reduction of the surface oxides by H_2 is almost complete in all cases before the transfer becomes possible. It has however to be mentioned that these findings are only valid for treatments at low temperatures. It has been shown in [11] that a heat treatment by heating to 650°C without soaking time in inert atmosphere (i.e. without oxidation) changes the surface composition

of the Cr-prealloyed material in such a way that deoxidation at low temperatures by hydrogen becomes impossible ("internal getter" effect).

CONCLUSIONS

As expected the artificial oxidizing of the powders and samples increases primarily the amount of oxides on the surface of the powder. Surprisingly the presence of oxygen-sensitive elements like chromium in prealloyed powder does not have a strong impact on oxidation at the temperature chosen here, and the predominant oxides formed are iron oxides. The situation may completely change when the oxidation is done at higher temperatures, allowing an enrichment of Cr on the former iron oxide surface (e.g. 600°C).

Stepwise sintering followed by consecutive analysis, combined with dilatometric + MS experiments, proved to be a powerful tool to understand the mechanisms during the sintering of these materials.

Although the initial oxygen contents of plain iron and Cr-alloyed material after artificial oxidation are comparable, the sintering experiments show markedly different behavior for the investigated materials.

For Fe-C the development of the mechanical properties and the interstitial content of the sintered material is indicated by the microstructure. The carbon and oxygen contents correspond in principle to the behavior in the dilatometric-MS experiment, although the carbon burn-off during the furnace experiment is an indicator that there is also a slight "internal getter" effect for the system Fe-C when heated rather fast. The carbon dissolution and the oxygen removal are slightly retarded for the artificially oxidized material. But if the sintering temperature is high enough the developed microstructures do not show significant differences any more, although the measured C-content is lower for the pre-oxidized materials due to the use of carbon as reducing agent. These small differences cannot be distinguished from the pearlite-ferrite ratio.

The Cr-prealloyed variant behaves differently. Here also the development of the mechanical properties runs in parallel with the microstructural development. But there are distinct differences to the Fe-C system. Here the first carbon dissolution, indicated by the first formation pearlite, is found at lower sintering temperatures in the artificially oxidized materials, although the removal of the surface oxides is not complete. This is different in the furnace sintering where "push-in-push-out" is applied compared to the dilatometric experiment done with constant heating rate. Therefore the high heating rate in the furnace may allow oxygen transfer reactions which are less likely in the dilatometric run. Therefore deoxidation in the furnace is somewhat different to that in the dilatometer, and also the temperature effects on hardness/impact energies are different. Also the sintering temperatures necessary to reach acceptably low oxygen contents are much higher for the artificially oxidized material. This coincides with significantly higher carbon loss and different microstructure compared with the reference material.

REFERENCES

[1] Chasoglou, D., Hryha, E., Norell, M., Nyborg, L: Applied Surface Science, vol. 268, 2013, p. 496
[2] Nyborg, L., Hryha, E. In: Advances in Powder Metallurgy & Particulate Materials 2014, Proceedings of the 2014 International Conference on Powder Metallurgy & Particulate Materials. Orlando, FL, MPIF, Princeton NJ, 2014, Vol. 2, p. 153
[3] Chasoglou, D., Hryha, E., Nyborg, L. In: Proc. Euro PM2009, Copenhagen, Denmark, Oct. 12-14, EPMA, UK 2009, Vol. 2, p. 181
[4] Chasoglou, D., Hryha, E., Nyborg, L. In: Proceedings of World PM2010, Florence,

EPMA, Shrewsbury UK, 2010, Vol. 2, p. 3
[5] Gierl-Mayer, C., Danninger, H., De Oro, R., Hryha, E. In: Advances in Powder Metallurgy and Part. Materials 2014; Proceedings of World PM Orlando, Florida May 18-22 2015, Eds. R.A. Chernenkoff, W.B. James, p. 05-74
[6] Gierl-Mayer, C., Danninger, H. In: Lecture at: International Conference on Sintering 2014, Dresden; 24.-28.08.2014
[7] Danninger, H., Nikolov, D., Leitner, G., Jaenicke-Rößler, K. In: Proc. Int. Conf. "Sintering '03", State College PA, 2003
[8] Kremel, S., Danninger, H., Yu, Y.: Powder Metall. Progress, vol. 2, 2002, no. 4, p. 211
[9] Danninger, H., Gierl, C.: Materials Chemistry and Physics, vol. 67, 2001, no. 1-3, p. 49
[10] Momeni, M., Gierl, C., Danninger, H.: Powder Metallurgy Progress, vol. 8, 2008, no. 3, p. 183
[11] Gierl-Mayer, C., Calderon, R., Danninger, H.: JOM, vol. 68, 2016, no. 3, p. 920

sciendo Powder Metallurgy Progress, Vol.19 (2019), No.1, p.023-033
http://dx.doi.org/10.1515/pmp-2019-0003

T DEPENDENCE OF THE MECHANICAL PROPERTIES ON THE MICROSTRUCTURAL PARAMETERS OF WC-Co

L. Emanuelli, A. Molinari, G. Arrighetti, G. Garoli

Abstract

The effect of binder content and WC grain size on the mechanical properties is widely investigated in literature. An increase in binder amount and WC grain size leads to a decrease in hardness and an increase in fracture toughness. Actually, these correlations are related to the influence of binder content and WC grain size through the contiguity and mean binder free path, which are the microstructural parameters that affect the mechanical properties. The aim of this study is to verify the dependence of the two microstructural parameters that govern the WC-Co mechanical behaviour, namely the contiguity and mean binder free path, on the mechanical properties of an extended range of WC-Co samples, which differ in terms of Co content and tungsten carbide grain size.

Keywords: WC-Co, mechanical properties, microstructure

INTRODUCTION

Mechanical properties of WC-Co are strongly related to chemical composition and microstructure. Increasing the metallic binder amount and the WC grain size (D_{WC}), hardness decreases and fracture toughness increases [1-3]. For this reason, by varying the two parameters it is possible to tailor the mechanical properties to the requirements of the specific application.

The methods used for the determination of WC-Co mechanical properties are defined by industry or national standards. Hardness, which is one of the most important properties being correlated to wear resistance of the material, is measured according to the ASTM B294 and ISO 3878 standards, using Rockwell A and Vickers as scales [1,4-6]. The fracture toughness, which is the resistance to crack propagation and is ideally independent on specimen dimension, geometry and surface finish, is usually correlated with KIC which refers only to plain strain fracture toughness. The measure of fracture toughness according to ASTM B771 and ASTM E399 standards is rather difficult, since pre-cracking stress is very similar to the critical stress intensity factor KIC [3] and therefore the introduction of the pre-crack by fatigue is quite a critical issue. A lot of works tried to define a new method for the determination of fracture toughness without any attractive effect by the industry because of the large size and complex geometry of the test samples. For this reason, the most common method for the determination of the fracture toughness has become the Palmqvist method [1, 3-8]. It is used for brittle materials and consists of the measurement of the length of the cracks formed at the four corners of a Vickers indentation.

L. Emanuelli, A. Molinari: Dpt. Industrial Engineering, University of Trento, Via Sommarive 9, 38123 Trento, Italy
G. Arrighetti, G. Garoli: Koner SRL, Via Bastida 3, 26100 Cremona, Italy

Considering the microstructure, the grain size of WC DWC in the sintered material, it is important to evaluate the quality of the sintering process and the effective role of the grain growth inhibitors (Cr3C2, VC and NbC) [3, 9-11]. The most common method used for the measurement of DWC is through quantitative metallography. As an example, the so called “linear intercept method” is used to quantify the grain size distribution and the mean DWC [12]. Another technique is the Jefferies method that calculates the WC average area and the equivalent diameter for the two-dimensional size of WC, without the possibility to define the size distribution [13]. Engqvist et al. proposed a new method to consider the three-dimensionality of the grain size [14].

The correlations between hardness and fracture toughness and cobalt content and carbide grain size are mostly due to the effect of two microstructural parameters that affect the mechanical behaviour:

- the carbide contiguity, which is a measure of the contacts between carbide particles and is defined as the surface area of carbide-carbide contacts as a fraction of the total contact area [3,5,15];
- the mean binder free path, which is the thickness of the binder layer between the carbides [3,5].

It is clear that on increasing the cobalt content contiguity decreases and the mean binder free path increases, increasing the fracture toughness but decreasing hardness [3]. The same effect on mechanical properties is obtained by an increase in carbide grain size, since contiguity still decreases and the mean binder free path increases.

The carbide contiguity and the mean binder free path are measured through the intercept method.

In this study, the correlations here described are investigated on several WC-Co wire drawing dies taken from industrial production. The cobalt content and WC particle size vary within small intervals, since the range of hardness/toughness combination required by this application, depending on the characteristics of the wire and of the process, is quite narrow. The aim of the work is to verify if even with small variations of the cobalt content and of the carbide grain size, hardness and Palmqvist fracture toughness may be correlated to the two microstructural parameters described above.

MATERIALS AND EXPERIMENTAL PROCEDURE

The cemented carbides investigated in this work are reported in Table 1.

A complete microstructural characterization was carried out. Murakami's reagent, which consists of 100 ml distilled water, 7g KOH and 7g K3[Fe(CN)6] [16], was used for selective etching of WC particles. The microstructure parameters, such as the mean linear intercept carbide size lav, DWC, contiguity (C) and mean binder free path (□), were measured by means of the linear intercept method [12] (Figure 1). They are defined by Eq. (1), (2), (3) and (4) [3, 5, 12, 14]

$$l_{av} = \frac{\sum l_i}{n} \quad (1)$$

$$D_{WC} = \frac{\sum l_i^4}{\sum l_i^3} \quad (2)$$

$$C = \frac{2 \cdot N_{L_{WC-WC}}}{2 \cdot N_{L_{WC-WC}} + N_{L_{WC-Co}}} \quad (3)$$

$$\lambda_{Co} = \frac{2 \cdot V_{Co}}{N_{L_{WC-Co}}} \quad (4)$$

Where li is the measured intercept length, n is the number of WC grains intercepted, NL is the number of WC-WC grain boundaries or WC-Co interfaces intercepted per unit length and VCo is the Co volumetric fraction.

Tab.1. Chemical composition and starting WC powder size of the studied industrial WC-Co.

Samples	WC (%)	Co (%)	Grain growth inhibitor (%)	WC powder size (µm)
A	93.7	6.0	0.3 Cr_3C_2	0.8
B	93.8	6.0	0.2 Cr_3C_2	0.8
C	93.5	6.0	0.5 Cr_3C_2	0.8
D	93.2	6.5	0.3 Cr_3C_2	0.8
E	93.2	6.5	0.3 Cr_3C_2	0.8
F	93.2	6.5	0.3 Cr_3C_2	0.8
G	93.2	6.5	0.3 Cr_3C_2	0.8
H	93.2	6.5	0.3 Cr_3C_2	0.8
I	93.3	6.5	0.3 Cr_3C_2	0.8
L	92.7	7.0	0.3 (W,Nb)C	1.1
M	92.7	7.0	0.3 VC	1.2
N	90.7	9.0	0.3 Cr_3C_2	0.8
O	91.0	9.0	-	1.0
P	90.7	9.0	0.3 Cr_3C_2	0.8
Q	91.0	9.0	-	1.0
R	88.0	12.0	-	1.0
S	88.0	12.0	-	1.0

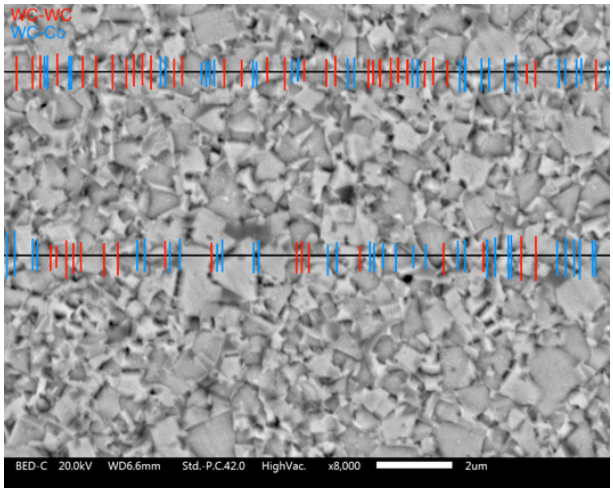

Fig.1. Example of the linear intercept method.

To get a statistically significant result, the test line has to intercept at least 20 grains and a minimum of 200 grains must be considered. C and λ were measured for each line and mean C and mean λ along with the respective standard deviations were calculated.

Vickers indentations with a load of 30Kg were used in order to measure the hardness (HV) and the fracture toughness (K_{IC}) of parts. Eq. (5) is used to determine hardness according to ISO 3878.

$$HV = 1.854 \cdot \frac{F}{\left(\frac{d_1+d_2}{2}\right)^2} \quad (5)$$

Where d_1 and d_2, in mm, are the two indentation diagonals and F is the load in Kg. HV is expressed in Kg/mm^2.

The fracture toughness KIC ($MPa\ m^{1/2}$) is determined by the Eq. (6), according to Palmqvist [1, 3-8].

$$K_{IC} = 0.0028 \cdot \sqrt{H} \cdot \sqrt{\frac{P}{\sum l_i}} \quad (6)$$

Where H is the Vickers hardness in N/mm^2, P is the load in N, and l_i are the crack lengths in mm.

RESULTS AND DISCUSSION

The D_{WC} and the mechanical properties of the investigated hardmetals are summarized in Table 2.

Tab.2. Mechanical properties of the investigated WC-Co.

Samples	WC (%)	Co (%)	Other carbide (%)	D_{WC} (µm)	l_{av} (µm)	HV30 (Kg/mm^2)	K_{IC} ($MPa\ m^{1/2}$)
A	93.7	6.0	0.3 Cr_3C_2	0.95	0.49 ± 0.25	1836 ± 16	9.95 ± 0.10
B	93.8	6.0	0.2 Cr_3C_2	0.74	0.44 ± 0.20	1887 ± 23	9.60 ± 0.12
C	93.5	6.0	0.5 Cr_3C_2	0.69	0.40 ± 0.19	1916 ± 12	9.70 ± 0.12
D	93.2	6.5	0.3 Cr_3C_2	0.82	0.44 ± 0.22	1912 ± 5	9.85 ± 0.03
E	93.2	6.5	0.3 Cr_3C_2	0.85	0.44 ± 0.23	1882 ± 17	9.73 ± 0.12
F	93.2	6.5	0.3 Cr_3C_2	0.83	0.47 ± 0.22	1844 ± 12	9.69 ± 0.12
G	93.2	6.5	0.3 Cr_3C_2	0.77	0.45 ± 0.22	1835 ± 23	9.82 ± 0.14
H	93.2	6.5	0.3 Cr_3C_2	0.70	0.43 ± 0.19	1864 ± 15	10.08 ± 0.08
I	93.3	6.5	0.3 Cr_3C_2	0.71	0.41 ± 0.20	1861 ± 7	9.77 ± 0.14
L	92.7	7.0	0.3 (W,Nb)C	1.07	0.53± 0.30	1691 ± 16	10.31 ± 0.08
M	92.7	7.0	0.3 VC	0.71	0.42 ± 0.21	1790 ± 17	9.95 ± 0.11
N	90.7	9.0	0.3 Cr_3C_2	0.83	0.44 ± 0.23	1653 ± 35	11.38 ± 0.55
O	91.0	9.0	-	1.27	0.61 ± 0.35	1534 ± 14	13.21 ± 0.39
P	90.7	9.0	0.3 Cr_3C_2	0.86	0.41 ± 0.22	1686 ± 11	11.23 ± 0.14
Q	91.0	9.0	-	0.97	0.50 ± 0.26	1607 ± 10	11.27 ± 0.26
R	88.0	12.0	-	1.60	0.58 ± 0.33	1404 ± 8	15.16 ± 1.55
S	88.0	12.0	-	1.45	0.54 ± 0.34	1404 ± 13	13.41 ± 0.70

The standard deviation of DWC is not reported in Table 2 since the 3D correction obtained by Eq. (2) does not imply a distribution and the associated scatter. For this reason it is also reported the lav that is the 2D evaluation of the grain size with its standard deviation.

Figure 2 shows the correlation between fracture toughness and hardness.

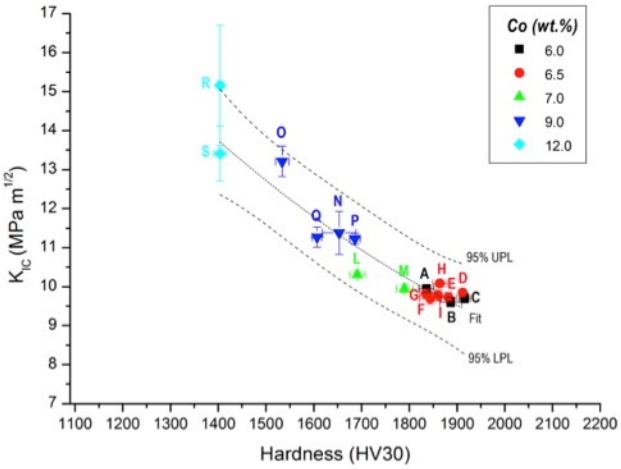

Fig.2. K_{IC} vs hardness.

As was expected [3-8], hardness and fracture toughness are inversely proportional.

Figures 3a and 3b show the influence of the Co content on the hardness and on the fracture toughness, respectively.

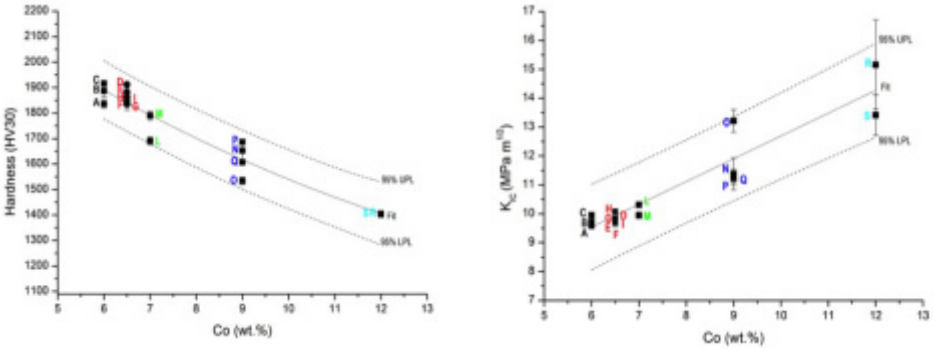

a) b)

Fig.3. (a) Hardness and (b) KIC vs Co content.

Both HV30 and K_{IC} are very similar for Co contents in the interval between 6 and 7 wt.% Co. Differently, increasing Co content up to 9% and 12% leads to a continuously decreasing hardness and an increasing fracture toughness, with a large scatter. The different properties of materials with the same amount of binder (6, 7 and 9%) are due to the influence of D_{WC} and that is shown in Fig.4.

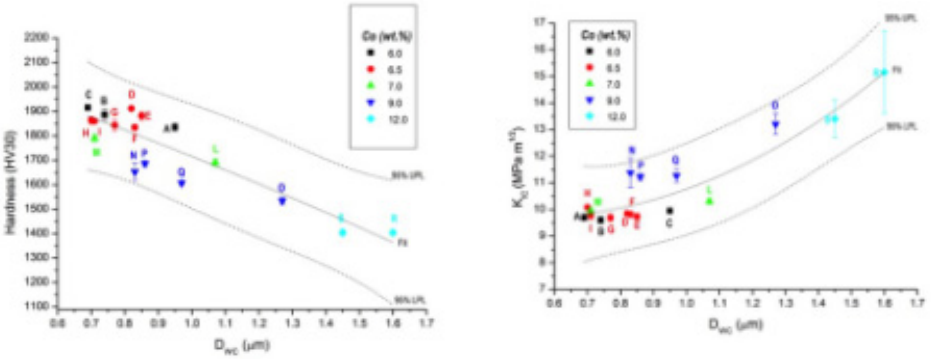

a) b)

Fig.4. (a) Hardness and (b) KIC vs DWC.

The Figure displays a general trend whereby the increase in D_{WC} decreases hardness and increases fracture toughness. Such a trend may be also recognized in specimens with 6.0, 7.0 and 9.0 wt.% Co, where the difference in D_{WC} is of the order of 0.4-0.5 μm. When the difference is smaller, as in specimens with 6.5 and 12.0 wt.% Co, the effect is not observed, because of the impossibility to define the D_{WC} standard deviation with the Eq. (2). Indeed, information regarding the grain size distribution homogeneity is given by the mean linear intercept grain size (l_{av}) obtained with the 2D Eq. (1) that presents a high standard deviation, as shown in Table 2. For this reason it is better to consider the l_{av} with its standard deviation in order to highlight the real influence of the grain size on the mechanical properties, as shown in Fig.5.

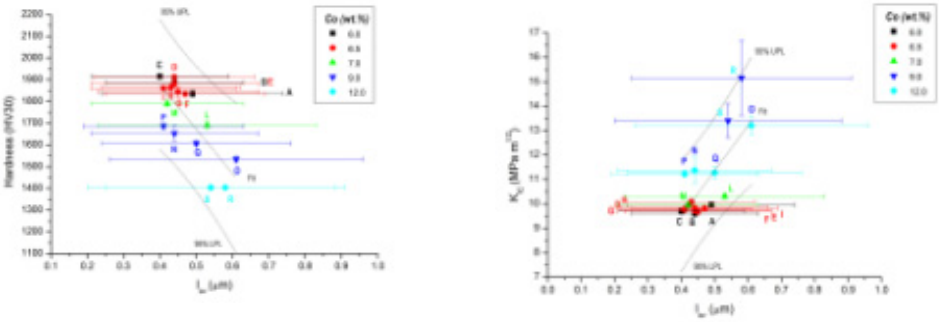

a) b)

Fig.5. (a) Hardness and (b) KIC vs lav.

It is evident that the high standard deviation of the l_{av} gives a difficult interpretation of the data. Considering grades with 6.5 and 12.0 wt.% of Co, the specimens present the same l_{av} leading to no differences in terms of mechanical properties. Otherwise, considering the material A respect to material B and C in grade with 6 wt.%, it is clear that the lower hardness and higher fracture toughness is due to a slightly higher l_{av}. The same consideration holds for grade with 9.0 wt.% of Co.

The contiguity and mean binder free path of the investigated cemented carbides are reported in Table 3.

Tab.3. Microstructure parameters of the different commercial WC-Co.

Samples	WC (%)	Co (%)	Other carbide (%)	D_{WC} (µm)	C (-)	λ_{Co} (µm)
A	93.7	6.0	0.3 Cr_3C_2	0.95	0.56±0.08	0.15±0.02
B	93.8	6.0	0.2 Cr_3C_2	0.74	0.56±0.04	0.13±0.01
C	93.5	6.0	0.5 Cr_3C_2	0.69	0.53±0.05	0.11±0.01
D	93.2	6.5	0.3 Cr_3C_2	0.82	0.62±0.12	0.16±0.04
E	93.2	6.5	0.3 Cr_3C_2	0.85	0.61±0.09	0.15±0.03
F	93.2	6.5	0.3 Cr_3C_2	0.83	0.53±0.09	0.14±0.03
G	93.2	6.5	0.3 Cr_3C_2	0.77	0.56±0.06	0.14±0.01
H	93.2	6.5	0.3 Cr_3C_2	0.70	0.52±0.06	0.13±0.02
I	93.3	6.5	0.3 Cr_3C_2	0.71	0.55±0.09	0.13±0.02
L	92.7	7.0	0.3 (W,Nb)C	1.07	0.50±0.09	0.16±0.03
M	92.7	7.0	0.3 VC	0.71	0.56±0.05	0.14±0.01
N	90.7	9.0	0.3 Cr_3C_2	0.83	0.54±0.13	0.18±0.06
O	91.0	9.0	-	1.27	0.51±0.11	0.24±0.05
P	90.7	9.0	0.3 Cr_3C_2	0.86	0.55±0.05	0.17±0.02
Q	91.0	9.0	-	0.97	0.54±0.11	0.21±0.05
R	88.0	12.0	-	1.60	0.44±0.11	0.26±0.06
S	88.0	12.0	-	1.45	0.48±0.06	0.29±0.4

The standard deviation of contiguity and mean binder free path is quite high for all the materials in comparison to the mean values. This may be attributed to the microstructure heterogeneity and to the microscope resolution that does not allow highly precise information about the distribution of binder between the carbides [3] to be obtained, as shown in Figure 5.

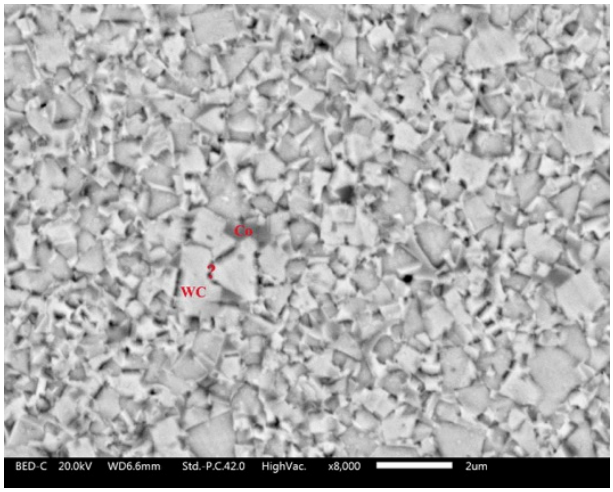

Fig.5. Example of the difficulties that occur in the measurement of the WC-WC grain boundaries and WC-Co interface.

The effect of the Co amount on contiguity and mean binder free path is reported in Fig.6.

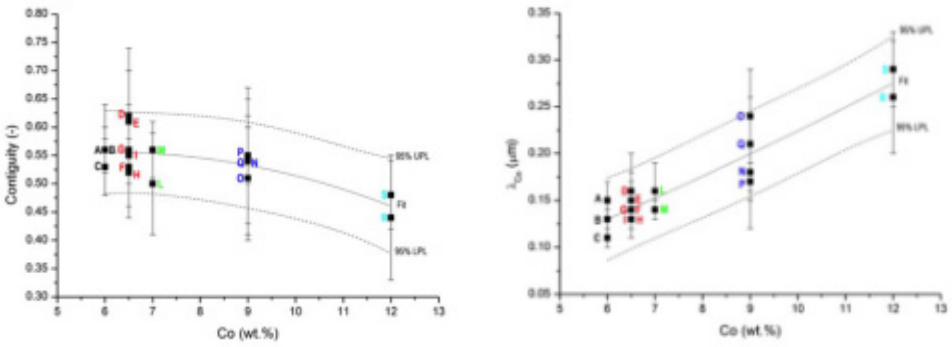

a) b)

Fig.6. (a) Contiguity and (b) mean binder free path vs Co content.

Figure 6a does not show a sharp influence of cobalt content on the contiguity since the difference between the mean values of materials with the lowest and the highest %Co is comparable to standard deviation. Otherwise, Figure 6b shows that the mean binder free path increases by increasing the Co content. Again, specimens with the same cobalt content display different contiguity and mean binder free path values because of the different D_{WC}.

Figures 7a and 7b show the dependence of contiguity and mean binder free path on D_{WC}.

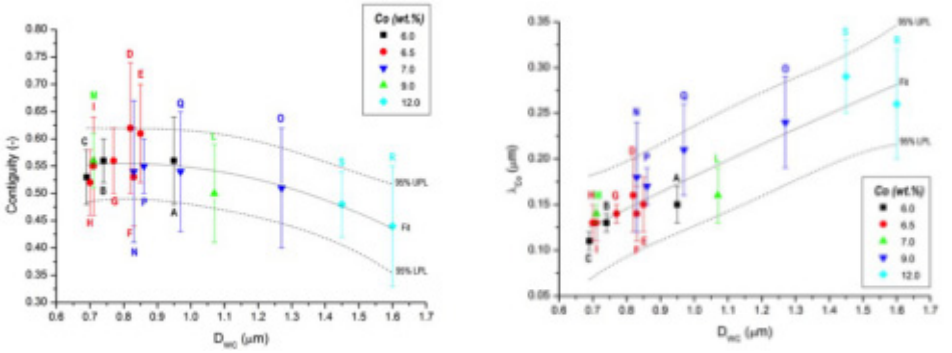

a) b)

Fig.7. (a) Contiguity and (b) mean binder free path vs DWC.

Figure 7a highlights that the effect of D_{WC} on the contiguity is significant only above 1 μm, again because of its high standard deviation. Analogously, as shown in Figure 7b, the increase of the mean binder free path with D_{WC} is significant above 1 μm.

From these results it is evident that the contiguity is characterized by a too high standard deviation that makes it impossible to define a clear dependence on Co content and D_{WC}. Otherwise, the influence of the Co content and D_{WC} on the mean binder free path is evident: a higher mean binder free path is obtained upon increasing the Co content and the D_{WC}.

It is now possible to correlate the two microstructural parameters that govern the WC-Co mechanical behaviour, namely the contiguity and mean binder free path, to the WC-Co mechanical properties.

Figure 8a and 8b show the influence of contiguity on hardness and fracture toughness, respectively.

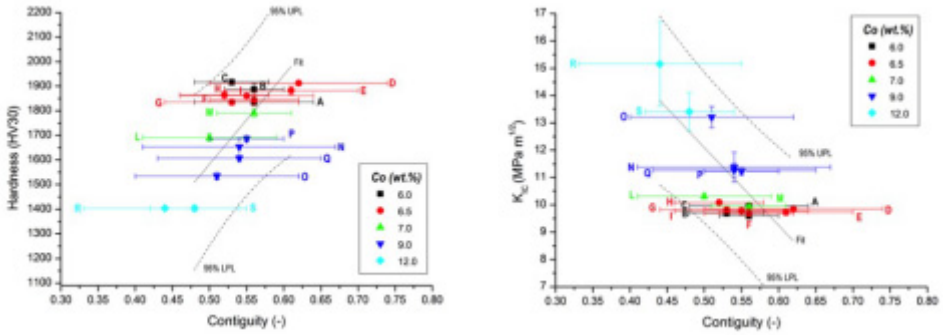

a) b)

Fig.8. (a) Hardness and (b) KIC vs contiguity.

The high standard deviation of the contiguity of the analyzed materials does not allow a clear correlation to be defined. The prediction lines with a 95% of confidence describe a trend, but the hardness and fracture toughness differences between specimens with the same contiguity are very large.

The influence of the mean binder free path on the hardness and the fracture toughness is visible in Fig.9.

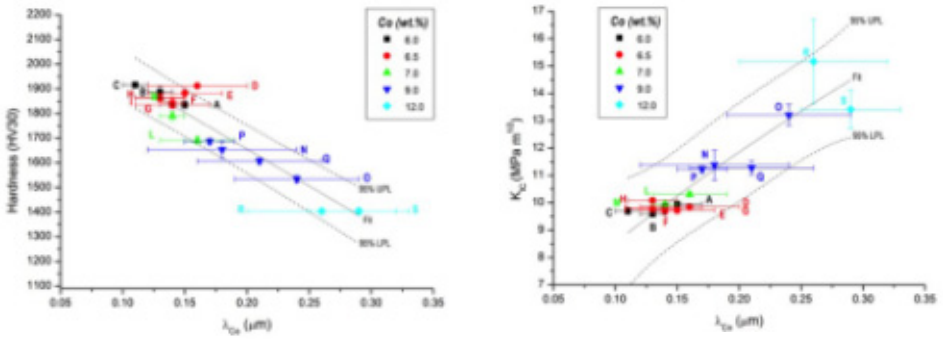

a) b)

Fig.9. (a) Hardness and (b) KIC vs mean binder free path.

The prediction lines up with 95% confidence to describe a sharp trend: a higher mean binder free path leads to a lower hardness and a higher fracture toughness. In general, there is a correspondence between hardness and λ_{Co} and between fracture toughness and λ_{Co}.

CONCLUSION

In this study, the influence of the contiguity and the mean binder free path on the hardness and the Palmqvist fracture toughness of a wide range of WC-Co samples were investigated on hardmetals applied to the production of wire drawing dies. The aim of the study is to verify if even materials having small differences of cobalt content and of carbide grain size, the hardness and Palmqvist fracture toughness may be clearly correlated to the two microstructural parameters described above.

The conclusion of this study may be summarized as follows:

1. The dependence of the carbide contiguity on Co content and D_{WC} results is weak because of the too large standard deviation of the contiguity values;
2. The correlation between the hardness and fracture toughness and the contiguity is therefore ambiguous.
3. The dependence of the mean binder free path on the Co content and D_{WC} is evident: the mean binder free path increases by increasing Co content and D_{WC};
4. The effect of the mean binder free path on the mechanical properties was therefore verified.

Among the two microstructural parameters investigated, only the mean binder free path displays the known correlation with hardness and fracture toughness. It increases upon increasing the cobalt content and the carbide particle size. The carbide contiguity does not display the known correlation with mechanical properties, since it is within ranges in a too narrow interval in the investigated materials, and the large scatter of data the expected trends are overwhelmed.

REFERENCES

[1] Brookes, KJA.: Hardmetals and other Hard Materials. 1992, United Kingdom: International carbide data
[2] Santhanam, AT., Tierney, P., Hunt, JL.: Properties and Selection: Non ferrous Alloys and Special Purpose Materials, 1990. ASM International. The Materials Information Company
[3] Upadhyaya, GS.: Cemented Tungsten Carbides: Production, Properties, and Testing. New Jersey : Noyes Publications, 1998
[4] Dobrzański, LA., Dolżańska, B.: Archives of Materials Science and Engineering, vol. 43, 2010, p. 87
[5] Jia, K., Fisher, TE., Gallois, B.: NanoStructured Materials, vol. 10, 1998, p. 875
[6] Schubert, WD., Neumeister, H., Kinger, G., Lux, B.: International Journal of Refractory Matals and Hard Materials, vol. 16, 1998, p. 133
[7] Shetty, DK., Wright, IG., Mincer, PN., Clauer, AH.: Journal of materials science, vol. 20, 1985, p. 1873
[8] Spiegler, R., Schmauder, S., Sigl, LS.: Journal of hard materials, vol. 1, 1990, p. 147
[9] Huang, SG., Liu, RL., Li, L., Van der Biest, O., Vleugels, J.: Int. Journal of Refractory Metals and Hard Materials, vol. 26, 2008, no. 5, p. 389
[10] Poetschke, J., Richter, V., Holke, R.: Int. Journal of Refractory Metals and Hard Materials, vol. 31, 2012, p. 218
[11] Zackrisson, J., Jansson, B., Uphadyaya, GS., Andren, HO.: International Journal of Refractory Metals and Hard Materials, vol. 16, 1998, no. 4-6, p. 417
[12] Bennett, EG., Roebuck, B.: NPL Measurement Good Practice Guide, vol. 22, 2000, p. 1368
[13] Jefferies, Z., Kline, AK., Zimmer, EB.: Trans AIME, vol. 57, 1916, p. 594
[14] Engqvist, H., Uhrenius, B.: International Journal of Refractory Metals & Hard

Materials, vol. 21, 2003, p. 31
[15] German, RM.: Sintering theory and practice. New York : John Wiley & sons, Inc., 1996
[16] Petzow, G.: Metallographic Etching. ASM Int Mater Park, 1999

sciendo Powder Metallurgy Progress, Vol.19 (2019), No.1, p.034-043
http://dx.doi.org/10.1515/pmp-2019-0004

POLYMORPHS OF NEODYMIUM NIOBATE AND TANTALATE THIN FILMS PREPARED BY SOL-GEL METHOD

H. Brunckova, Ľ. Medvecký, E. Múdra, A. Kovalčiková

Abstract

Neodymium niobate NdNbO4 (NNO) and tantalate NdTaO4 (NTO) thin films (~100 nm) were prepared by sol-gel/spin-coating process on Pb(Zr0.52Ti0.48)O3/Al2O3 substrates with annealing at 1000°C. The precursors of films were synthesized using Nb or Ta tartrate complexes. The XRD results of NNO and NTO films confirmed tetragonal T-NdNbO4 and T-NdTaO4 phases, respectively, with traces of monoclinic M-NdNbO4 and M´-NdTaO4. The surface morphology and topography were investigated by SEM and AFM analysis. NTO was smoother with roughness 5.24 nm in comparison with NNO (6.95 nm). In the microstructure of NNO, small spherical (~ 20-50 nm) T-NdNbO4 and larger needle-like particles (~100 nm) of M-NdNbO4 phase were observed. The compact clusters composed of fine spherical T-NdTaO4 particles (~ 50 nm) and cuboidal M´-NdTaO4 particles (~ 100 nm) were found in NTO. The results of this work can contribute to formation of different polymorphs of films for the application in environmental electrolytic thin film devices.

Keywords: sol-gel, thin films, NdNbO4, NdTaO4, polymorphs, microstructure

INTRODUCTION

Neodymium orthoniobate NdNbO4 (NNO) and orthotantalate NdTaO4 (NTO) thin films with fergusonite structure have attracted a great deal of attention due to their interesting physical properties, such as high dielectric constants, electro-optical, photoelastic, photocatalytic and luminescent properties as well as good mechanical and chemical stability [1,2]. For lanthanide Ln (Ln = Nd, Sm, Eu and Gd) orthoniobates, there are two crystalline forms, the low temperature M-phase isostructural with monoclinic form of the fergusonite and the T-phase corresponding to tetragonal scheelite. The transition between the two phases occurs reversibly in the range 500-800°C [3]. The NdTaO4 crystallize in monoclinic form, besides their ability to posses two-fergusonite-type structures, first known as M-type (I2/a) and second called M´-type (P2/a). NdTaO4 exist in three polymorphs (T, M and M´) [4-7].

Helena Brunckova, Ľubomír Medvecký, Erika Múdra, Alexandra Kovalčiková: Institute of Materials Research of Slovak Academy of Sciences, Watsonova 47, 040 01 Košice, Slovak Republic

NNO and NTO precursors of thin films can be prepared by different methods: conventional solid state reaction (SSR) [8,9], hydrothermal [10] and sol-gel [1,2]. The sol-gel method has been used to prepare NdNbO4 and NdTaO4 at low temperature [1]. The NNO precursor powders were prepared using the sol-gel method and obtained at 900°C single NdNbO4 phase [2]. The nanocrystalline NNO powders were prepared by sol-gel process and annealing at 1000°C [11]. High quality NTO films on silica glass substrate were prepared by modified sol-gel process and heating at 1200°C with a single monoclinic M′ phase and NTO film composed of M′-type and tetragonal T-type NdTaO4 [12].

Recently, several groups published studies on the relationship between electrical behavior and phase and crystallographic orientation by the introduction of buffer layers such as SrRuO3, LaNiO3, SrTiO3, (La,Sr)MnO3, (La,Sr)CoO3 as an effective method to improve properties of thin films [13,14]. The significant impact of SrTiO3 [13] or (La,Sr)CoO3 [14] acting as buffer layers on structural, microstructural and ferroelectric properties for (Bi,Nd)4Ti3O12 or (Pb,Ca)TiO3 thin films was clearly revealed. By using PbTiO3 and (Pb0.72La0.28)TiO3 or Pb(Zr0.52Ti0.48)O3 (PZT) interlayer it was possible to control the PZT film orientation [15,16].

In this work, we demonstrate a method to prepare novel NdNbO4 and NdTaO4 thin films from polymeric Nb and Ta-tartrate solutions by sol-gel/spin-coating process. We also report the structural properties and morphology of NNO and NTO thin films deposited on the alumina substrates with PZT interlayer and annealed at 1000°C. The results of this work can contribute to the fabrication of these films for application in environmental electrolytic thin film devices.

EXPERIMENTAL

NdNbO4 (NNO) and NdTaO4 (NTO) precursors were prepared by modified polymeric complex sol-gel method [17]. The novel NNO or NTO sol precursors were synthesized from Nd(NO3)3 and Nb- or Ta-tartrate complex in solvent (ethylene glycol, (EG)) with molar ratio of Nd/Nb or Nd/Ta = 1/1. The mole ratio of tartaric acid (TA):EG = 3:1. After homogenization at 80°C, the solutions were stirred, heated at 130°C for 5 hours with the formation of transparent viscous sols. Basic (0.5 M) sols were diluted in stabilization solution (n-propanol). The sols remained stable at room temperature for two months. Pb(Zr0.52Ti0.48)O3 (PZT) sol was prepared by sol-gel method [18]. The raw materials, lead acetate trihydrate and zirconium acetylacetonate were dissolved separately at a temperature of 80°C in glacial acetic acid in two closed flasks. The solutions were dehydrated at 105°C for 2 hours and, after cooling to 80°C, they were mixed with titanium orthotetrabutylate Ti(OR)4 in the required ratio of Pb:Zr:Ti = 1:0.52:0.48. After adding ethylene glycol at the temperature 80°C, an orange sol was formed. The PZT sol concentration after dilution with n-propanol was 1.0 M.

NdNbO4 and NdTaO4 thin films were prepared from the sols synthesized in the stoichiometric ratio and deposited on Al2O3 substrates. The alumina substrates were spin-coated with PZT sol precursor at 2000 rpm for 30 s (PZT interlayer). Single NNO or NTO film layer was deposited on PZT/Al2O3 substrate with a drying step at 110°C for 3 min and calcined at 400°C for 3 min. The coating cycling was repeated three times to obtain three layers of thin films. The final 3-layered NNO and NTO films were annealed at 1000°C for 1 hour in air.

The thermal decomposition of gels were analysed by differential scanning calorimetry, thermogravimetric analysis (JUPITER STA 449-F1 NETZSCH). The phase composition of films was determined by X-ray diffraction analysis (XRD), (a model X' Pert Pro, Philips, The Netherlands) using CuKα radiation. The Raman spectra were

collected by Raman spectroscopy (HORIBA BX 41TF). The surface of film microstructures were characterized using SEM equipped with a focused ion beam (FIB-SEM), (Auriga Compact, Carl Zeiss Germany). Surface topography and root mean square roughness of films were characterized by atomic force microscopy (AFM, Aicon).

RESULTS AND DISCUSSION

The TG and DSC curves of prepared xerogels heated to 1300°C in air are shown in Fig.1. The small weight losses of 6% at temperatures up to 200°C are due to the evaporation of remains of water residuals and ethylene glycol. It was shown that all chemical reactions involving weight loss, such as decomposition of organic polymeric network, finished below 500°C. In Figure 1, the exothermic peaks at 323 and 344°C (NNO) could be attributed to thermal decomposition of tartrate complexes with a corresponding approx. 47.3% (NNO) weight loss. The formation of amorphous oxides started above 400°C with small exo-effects. The presence of small exothermic peaks between 450 and 600°C is the result of the combustion of residual carbon and following crystallization of NdNbO4 phase at 640°C (fluorite tetragonal phase unknown structure denoted as T′ when it is prepared from amorphous) [1]. The exothermic effect above 890°C (NNO) corresponds to the transformation from T′ to the stable T or M phase. In the DSC curve of NNO, the broad and distinct endothermic peak above 1090°C characterizes the T-M transformation of NdNbO4. The last approximately 6% weight loss on TG curve between 900 to 1300°C relates to the above transformations. On the basis of TG analysis, the total weight losses were about 53% (NNO). DSC analysis showed the broad exothermic peaks at 328 and 625°C (NTO) which correspond to organic removal by oxidation with weight losses of about 40.0% (NTO). The two small exothermic peaks at 900 and 994°C (NTO) were observed. The first exo-peak is caused by crystallization of T′ phase and the second correspond to the residual carbon oxidation. The next exothermic peak at 1070°C (NTO) related to transformation from metastable fluorite T′ structure to T or M′ phase. The distinct endothermic peak above 1200°C characterizes the T-M transformation of NdTaO4. The three stage of weight losses above 1200°C are visible on TG curves of NTO xerogel over the temperature range 200°C, 700°C and 1200°C. From TG analysis is resulted that the total weight losses were 51% (NTO).

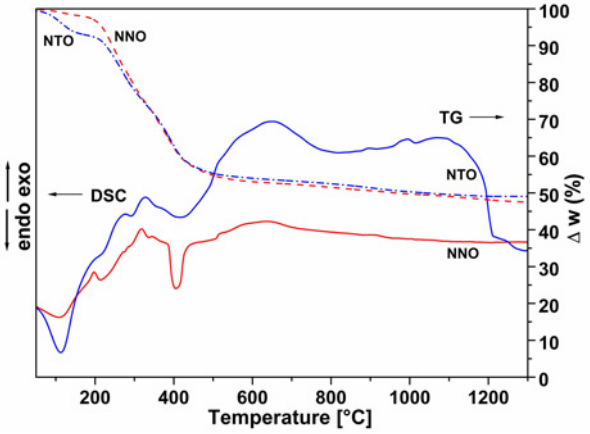

Fig.1. DSC and TG curves of $NdNbO_4$ (NNO) and $NdTaO_4$ (NTO) gel precursors.

The XRD diffractograms of NNO and NTO thin films deposited on PZT/Al_2O_3 substrates and annealed at 1000°C are shown in Fig.2. The XRD analyses verified formation of the monoclinic ZrO_2 (JCPDS 83-0944) in PZT, tetragonal T-$NdNbO_4$ (81-1974) and monoclinic M-$NdNbO_4$ (32-0680) in NNO, tetragonal T-$NdTaO_4$ (16-0745) and monoclinic M´-$NdTaO_4$ (83-0408) phases in NTO. From XRD patterns it resulted that the major phase is T-$NdNbO_4$ in NNO. Lanthanide tantalates usually crystallize in three different structures at room temperature [19,20]. One belongs to I2/a symmetry or M-type (fergusonite structure), the other is P2/a symmetry or M´-type, which is true equilibrium phase at room temperature with the M-type modification and another is the high temperature tetragonal phase of the scheelite structure or T-type. As shown in Fig. 2, the NTO film coincides with tetragonal T-$NdTaO_4$ and monoclinic M´-$NdTaO_4$ phases. From XRD patterns it resulted that the tetragonal phase transforms to M phase in $NdNbO_4$ films or M´ phase in $NdTaO_4$ films.

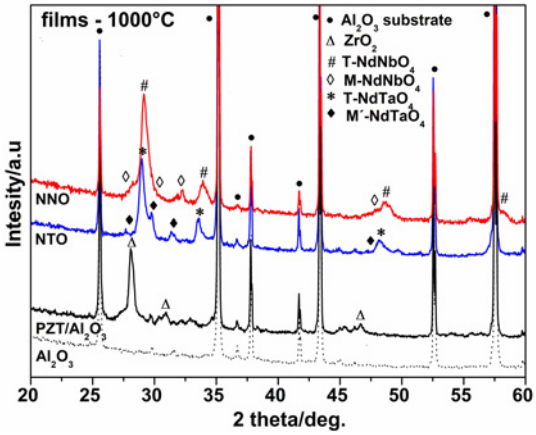

Fig.2 XRD patterns of $NdNbO_4$ and $NdTaO_4$ thin films on PZT/Al_2O_3 substrates after annealing at 1000°C.

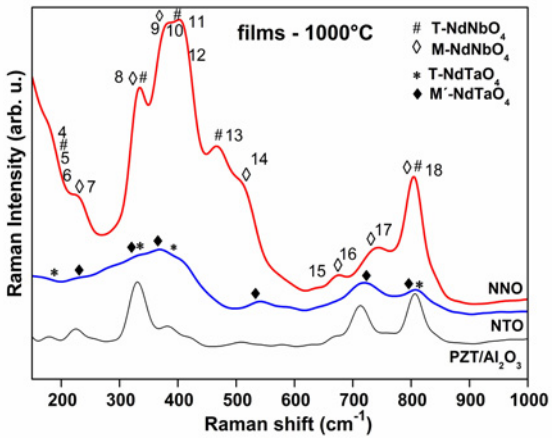

Fig.3. Raman spectra of $NdNbO_4$ and $NdTaO_4$ thin films on PZT/Al_2O_3 substrates after annealing at 1000°C.

Raman spectra of the films after annealing at 1000°C are shown in Fig. 3. The 18 optical Raman active phonon modes are expected [21,22]. Two dominant bands at 330 cm^{-1} and 800-805 cm^{-1} were clearly identified in all films. These bands are assigned as the bending and stretching modes of MO_6 ($M=Nb^{5+},Ta^{5+}$) octahedron, respectively. The intense three peaks at 331, 420 and 465 cm^{-1} or peak between 600 and 850 cm^{-1} are visible in NNO. Similar doublets assigned tetragonal T-$NdTaO_4$ and monoclinic M´-$NdTaO_4$ structure was found in the spectra of NTO thin film. Frequencies in range 230-450 cm^{-1} are influenced by Nd^{3+} cation displacements. 550-850 cm^{-1} range could be assigned to the Nb-O or Ta-O stretching modes essentially involving oxygen atom shifts [22]. Two new peaks in the around 537 and 730 cm^{-1} in $NdTaO_4$ film appeared and correspond to luminescence spectra. The phase composition and list of the observed frequencies of the Raman-active bands of NNO and NTO films were included in Table 1.

Tab.1. Phase composition and a list of the observed frequencies of the Raman-active bands of $NdNbO_4$ and $NdTaO_4$ films annealed at 1000°C.

Films	NNO	NTO
Phase composition	Tetragonal T-$NdNbO_4$ (81-1974) Monoclinic M-$NdNbO_4$ (32-0680)	Tetragonal T-$NdTaO_4$ (16-0745) Monoclinic M´-$NdTaO_4$ (83-0408)
Raman mode (Wavenumbers [cm^{-1}])	4 (180.1), 7 (229.4), 9 (331.0), 11 (377.2), 12 (407.2), 14 (471.2), 17 (674.5), 18 (803.1)	4 (174.2), 7 (210.2), 9 (323.4), 11 (372.4), 12 (403.2), 14 (490.3), 17 (678.2), 18 (810.1)

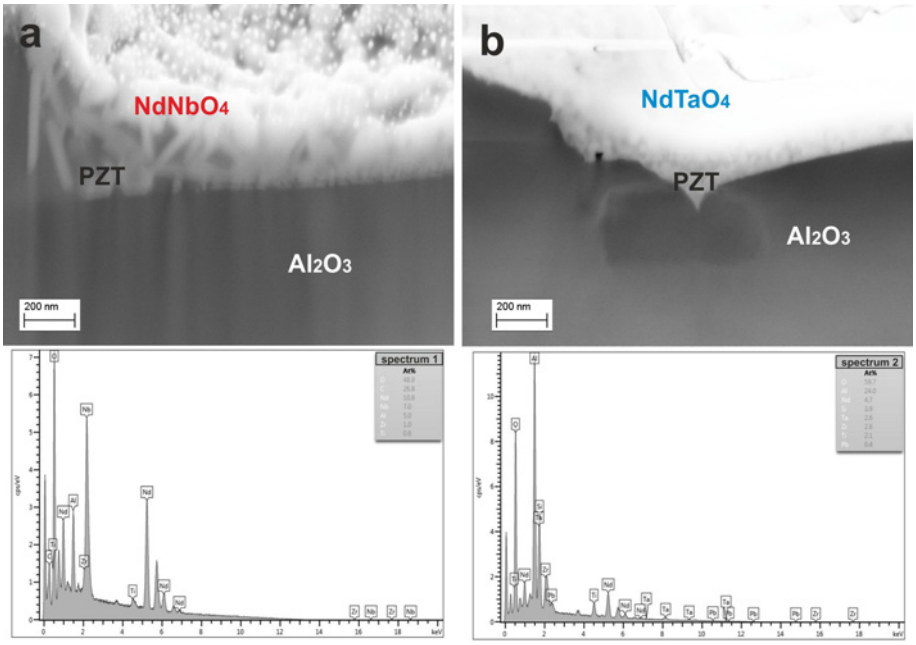

Fig. 4 FIB-SEM cross-section microstructures of (a) NNO/PZT/Al_2O_3, (b) NTO/PZT/Al_2O_3 thin films and EDS spectra 1 and 2.

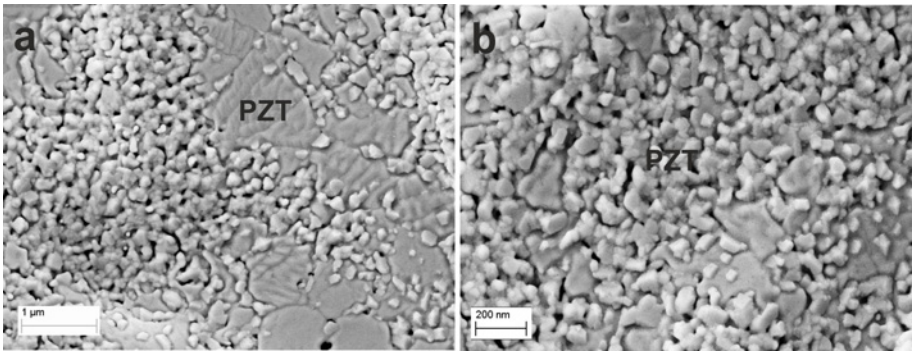

Fig. 5 SEM surface microstructures of PZT interlayer on Al_2O_3 substrate annealed at 1000°C with different resolution of (a) 1 μm and (b) 200 nm.

The cross-section microstructure of NNO (Fig.4) thin film deposited on PZT/Al_2O_3 substrate was characterized using SEM equipped with a focused ion beam (FIB-SEM). From image analysis of film it resulted that the NNO (Fig. 4a), NTO (Fig.4b) films and PZT layer thickness was ~100 and ~50 nm, respectively. EDS analyses demonstrate the distribution of elements across NNO (spektrum 1) and NTO (spektrum 2) films and results confirm the presence of Nd, Nb or Ta, in the films, Pb, Zr, Ti from PZT interlayer and Al, O from Al_2O_3 substrate.

Fig. 5a,b demonstrates the SEM micrographs of PZT interlayer on Al_2O_3 substrate. The film microstructures contained two phases (monoclinic ZrO_2 and pyrochore PZT). Pyrochlore $Pb_2(Zr, Ti)_2O_7$ phase [23] occurs at 29° (222), 33° (400) and 45°(200) and was not confirmed by XRD in Fig. 2 (one PZT layer - only 50 nm thickness).

The SEM micrographs of the NNO and NTO thin films are shown in Fig. 6. It was observed that the particles of the ceramic films were dense and uniform at the temperature 1000°C. The microstructure of NTO (Fig. 6b) film composed of $NdTaO_4$ was smoother than NNO film (Fig. 6a). The heterogeneous microstructure of the NTO is characterized by the bimodal particle size distribution and contains smaller spherical tetragonal $NdTaO_4$ (~ 30-50 nm) and bigger monoclinic $NdTaO_4$ particles of about ~100 nm. EDS analyses demonstrate the distribution of elements across NNO (spektrum 1) and NTO (spektrum 2) films and results confirm the presence of Nd, Nb or Ta, in the films. We described that 3 layers were deposited on substrate. We observed this preparation step in the final structures of perovskite interlayer $Pb(Zr_{0.52}Ti_{0.48})O_3/Al_2O_3$ and pyrochlore $NdNbO_4/Pb(Zr_{0.52}Ti_{0.48})O_3/Al_2O_3$ or $NdTaO_4/Pb(Zr_{0.52}Ti_{0.48})O_3/Al_2O_3$ films. The thickness of $Pb(Zr_{0.52}Ti_{0.48})O_3$ (PZT) and $NdNbO_4$ or $NdTaO_4$ thin films were ~ 50 and ~ 100 nm, respectively.

The 2D and 3D AFM micrographs of the PZT interlayer, NNO and NTO thin films are shown in Figs. 7 and 8. The monoclinic $NdNbO_4$ phase shows type ferroelasticity rubber-like behavior (pseudoelasticity) found in NNO film (Fig. 8) and domain structure was observed in NNO precursor [24,25]. As shown in Fig. 8, the AFM image illustrates that average particle size in NTO film (~ 50-100 nm). The root mean square (R_q) surface roughness values of the films were calculated as 6.95 nm for NNO, 5.24 nm for NTO and 24 nm for PZT layer on Al_2O_3 substrate. The structural properties of NNO and NTO films are depending on their phase composition.

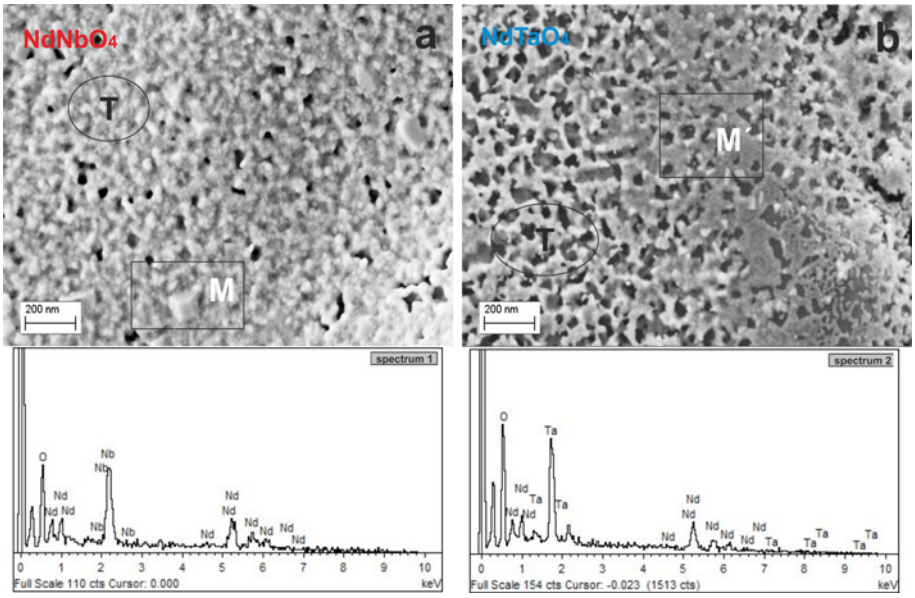

Fig. 6 SEM surface microstructures of $NdNbO_4$ (spektrum 1) and $NdTaO_4$ (spektrum 2) thin films annealed at 1000°C and EDS spectra.

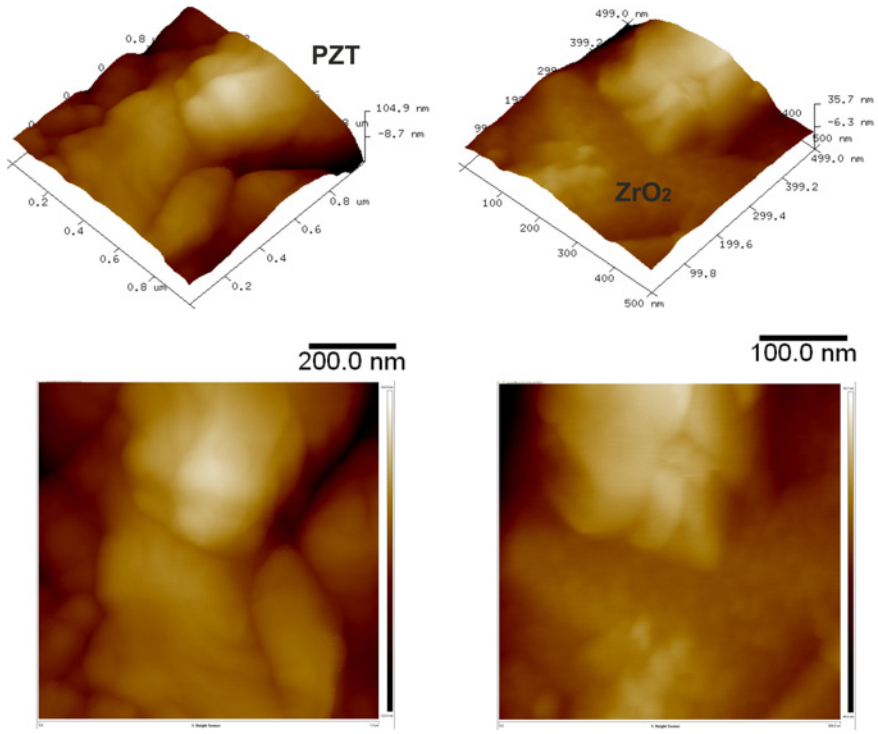

Fig.7. 2D and 3D AFM surface topography of PZT/Al_2O_3 substrate annealed at 1000°C.

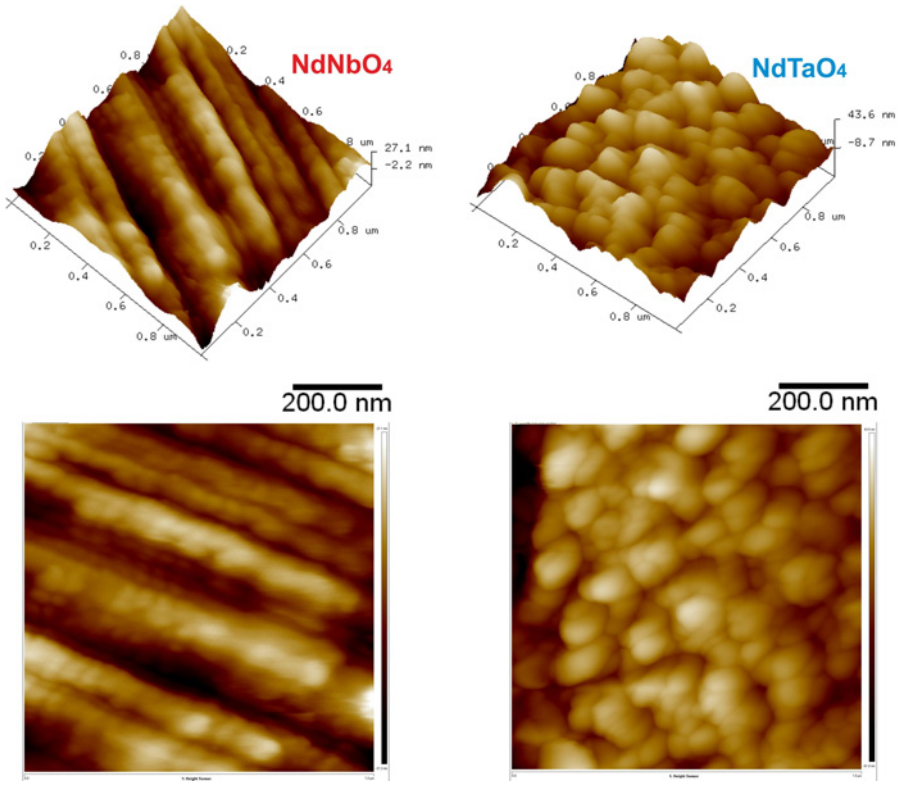

Fig.8. 2D and 3D AFM surface topography of $NdNbO_4$ and $NdTaO_4$ thin films annealed at 1000°C.

In the sol-gel process, the surface and properties of the films were crucially affected by the amount of carboxylic (citric or tartaric) acid [1]. The addition of tartaric acid could significantly increase the particle size and change the surface of NNO and NTO films. The shape and size of nanoparticles play an essential role in determining the electrolytic properties. The thermal evolution for NNO and NTO films showed that crystal phases are formed up to 1000ºC, while single well-crystallized M-$NdNbO_4$ or M´-$NdTaO_4$ materials are obtained in temperatures higher than 1000ºC. In future work, the influence of the annealing time will be investigated for the NNO and NTO films: a longer time is necessary to obtain thin films in the single monoclinic structure for application in environmental electrolytic thin film devices.

CONCLUSIONS

In conclusion, we have developed novel neodymium niobate and tantalate thin films using tartrate solutions. The ceramic $NdNbO_4$ (NNO) and $NdTaO_4$ (NTO) thin films (~100 nm) were prepared by sol-gel/spin-coating method on Al_2O_3 substrates with $Pb(Zr_{0.52}Ti_{0.48})O_3$ (PZT) interlayer and annealed at 1000°C.

The structural characterization of the films demonstrates strong different phase formation in NNO film in comparison with NTO. XRD results confirmed the major presence of tetragonal T-$NdNbO_4$ or T-$NdTaO_4$ and minor monoclinic M-$NdNbO_4$ or M´-$NdTaO_4$ phases in NNO and NTO thin films. The needle-like sharp features were identified

in the heterogeneous microstructure of $NdNbO_4$ film, which is different as compared with the Nd tantalate film composed of spherical particles (tetragonal $NdTaO_4$) and cuboidal (monoclinic $NdTaO_4$ phase).

It is found that the carboxylic acid has a strong morphological directing function. By using tartaric acid as the complexing agent, spherical and needle-like or cuboidal-shaped nanoparticles with different sizes and crystal phases could be obtained. The method reported here provides a new approach to preparing uniform NNO and NTO films. The results of this work can contribute to the fabrication of these films for application in environmental electrolytic thin film devices.

Acknowledgement

This work was supported by the Grant Agency of the Slovak Academy of Sciences through project No. 2/0036/17.

REFERENCES

[1] Mather, SA., Davies, PK.: J. Am. Ceram. Soc., vol. 78, 1995, p. 2737.
[2] Mei, QJ., Li, CY., Guo, JD., Zhao, LP., Wu, HT.: Ceram. Int., vol. 41, 2015, p. 907.
[3] Loiko, PA., Dymshits, OS., Alekseeva, IP., Zhilin, AA., Tsenter, MY., Vilejshikova, EV., Bogdanov, KV., Mateos, XK., Yumashev, KV.: J. Luminesc., vol. 179, 2016, p. 64.
[4] Siqueira, KPF., Carmo, AP., Bell, MJV., Dias, A.: J. Luminesc., vol. 138, 2013, p. 133.
[5] Ferrara, Ch., Mancini, A., Ritter, C., Malavasi, L., Tealdi, C.: J. Mater. Chem. A, vol. 3, 2015, p. 22258.
[6] Siqueira, KPF., Dias, A.: Mater. Res., vol. 17, 2014, p. 167.
[7] Titova, YA., Sych, AM., Sokolov, AN., Kapshuk, AA., Markiv, VY., Belyavina, NM.: J. Alloys Compd., vol. 311, 2000, p. 252.
[8] Zhang, P., Song, Z., Wang, Y., Han, Y., Dong, H., Li, L.: J. Alloys Compd., vol. 581, 2013, p. 741.
[9] Song, Z., Zhang, P., Wang, Y., Li, L.: J. Alloys Compd., vol. 583, 2014, p. 546.
[10] Hirano, M., Dozono, H.: Mater. Res. Bull., vol. 50, 2014, p. 213.
[11] Siqueira, KPF., Lima, PP., Ferreira, RAS., Carlos, LD., Bittar, EM., Matinaga, FM., Paniago, R., Moreira, RL., Dias, A.: J. Phys. Chem. C, vol. 119, 2015, p. 17825.
[12] Lu, Y., Tang, X., Yan, L., Li, K., Liu, X., Shang, M., Li, Ch., Lin, J.: J. Phys. Chem. C, vol. 117, 2013, p. 21792.
[13] Peng, H., Zhang, Y., Zhou, Y. C.: Prog. Nat. Sci.: Mater. Int., vol. 22, 2012, p. 219.
[14] Pontes, DSL., Pontes, FM., Pereira-da-Silva, MA., Zampieri, M., Chiquito, AJ., Pizani, PS., Longo, E.: Ceram. Int., vol. 40, 2014, p. 4085.
[15] Velu, G., Haccart, T., Jaber, B., Re`miens, D.: J. Vac. Sci. Technol. A: Vac. Surf. Films, vol. 16, 1998, p. 2442.
[16] Li, DH., Lee, ES., Chung, HW., Lee, SY.: Appl. Surf. Sci., vol. 252, 2006, p. 4541.
[17] Brunckova, H., Medvecky, L., Briancin, J., Durisin, J., Mudra, E., Sebek, M., Kovalcikova, A., Sopcak, T.: Mater. Lett., vol. 165, 2016, p. 239.
[18] Brunckova, H., Medvecky, L., Briancin, J., Saksl, K.: Ceram. Int., vol. 30, 2004, p. 453.
[19] Xiao, X., Yan, B.: J. Mater. Res., vol. 23, 2008, p. 679.
[20] Wang, J., Chong, X., Zhou, R., Feng, J.: Scripta Mater., vol. 126, 2017, p. 24.
[21] Siqueira, KPF., Dias, A.: Mater. Res., vol. 17, 2014, p. 167.
[22] Siqueira, KPF., Moreira, RL., Dias, A.: Chem. Mater., vol. 22, 2010, p. 2668.
[23] Yue, J., Leung, M., Haemmerle, E., Hodgson, M., Li, G., Gao, W.: J. Alloys Compd.,

vol. 470, 2009, p. 465.
[24] Tsunekawa, S., Takei, H.: Phys. Status Solidi A, vol. 50, 1978, p. 695.
[25] Kuroiwa, Y., Nozawa, K., Ikegami, J., Shobu, T., Noda, Y.: J. Korean Phys. Soc., vol. 32, 1998, p. 84.

sciendo Powder Metallurgy Progress, Vol.19 (2019), No.1, p.044-052
http://dx.doi.org/10.1515/pmp-2019-0005

DIE WALL - VS. BULK LUBRICATION IN WARM DIE COMPACTION: DENSITY, MICROSTRUCTURE AND MECHANICAL PROPERTIES OF THREE LOW ALLOYED STEELS

M. Zadra, L. Girardini, G. Pederzini, G. Patuelli, M. Piva, S. Bordin, L. De Mitri, A. Popolizio, I. Cristofolini, A. Molinari

Abstract
The influence of die wall lubrication during warm die compaction on densification, microstructure and mechanical properties of three low alloy ferrous powders was investigated. Specimens were sintered at 1250°C. Die wall lubrication leads to higher green and sintered density and enhances the dimensional stability. It does not affect the microstructure of the matrix, while pores are smaller and more rounded than in bulk lubricated specimens. In TRS tests, both strength and deformation are higher in die wall lubricated specimens than bulk lubricated ones.
Keywords: die wall lubrication; warm die compaction

INTRODUCTION

It's well known that the mechanical properties of materials produced with the press-and-sintering technology are strongly affected by the residual porosity. Pores cause local stress enhancement and strain localization, and this effect is dependent on their amount, size, morphology and distribution in the cross section.

The green density achievable by uniaxial cold compaction is limited by the powder compressibility and by the geometry of the parts. The compressibility of the powder is determined by several parameters: morphology and size distribution of the particles, chemical composition, surface quality, and a great effect is due to the presence of the lubricant. Lubricant admixed to the powder (bulk lubrication) reduces the frictional forces opposing densification, but at the same time it reduces the maximum achievable density (the theoretical density of the powder/lubricant mix).

Warm compaction increases the green density 0.2-0.3 g/cm3 above that of cold compaction, with a corresponding effect on the sintered density. Pores in the green parts are smaller, more rounded and homogeneously distributed than in cold compaction [1]. This is obtained by heating up the powder, the feeding system and the compaction tools at 120-140°C, but the theoretical density is still decreased by the presence of the lubricant, even if in a smaller amount than in cold compaction. Die warm compaction is an "easier" alternative to warm compaction, whereby only the die is heated up [2-7]; it still involves bulk lubrication.

Mario Zadra, Luca Girardini: K4Sint Srl, via Dante 300, 38057 Pergine Valsugana, (TN), Italy
Gianluca Pederzini, Gianluca Patuelli, Massimiliano Piva: Powder Metal B.U. – Sacmi Imola S.C., via Selice 17, 40026, Imola (BO), Italy
Stefano Bordin, Luigi De Mitri: TFM SpA, via del Concilio 3, 35035 Lissaro di Mestrino (PD), Italy
Antonio Popolizio, Ilaria Cristofolini, Alberto Molinari: University of Trento, via Sommarive 9, 38123 Povo di Trento, Italy

In die wall lubrication compaction the lubricant is not mixed to the powder, but it is deposited on the surfaces of the die and punches every stroke during cold compaction. In this case, the theoretical density in compaction is that of the powder and a greater green density, and in turn a greater sintered density can be attained.

Die wall lubrication has been investigated for decades. In 1987, James [8] demonstrated the potential of die wall lubrication with trials carried out in an industrial environment, highlighting the virtual elimination of lubricant burnt off, the lower furnace operating costs and the avoidance of contamination of PM components leading to the enhancement of sintered density. Other papers investigated the subject showing the positive effects on density, ejection forces and mechanical properties, in comparison to cold and warm compaction [9-15]. The critical issue is the reliability of the solutions applied to lubricate the tooling surfaces and its impact on the press productivity. Die wall lubrication is still a stimulating challenge that might offer to Powder Metallurgy significant advantages not only in terms of density-mechanical properties relationship, but also in terms of environmental sustainability, due to the elimination of the lubricants and the emissions resulting from their elimination during sintering.

In this paper, the results of a study on the sintering shrinkage, the microstructure and the mechanical properties of three low alloyed steels produced by warm die compaction with bulk lubrication and by die wall lubrication, and sintered at high temperature, are presented. In a previous preliminary work, the authors of the present paper confirmed the effectiveness of die wall lubrication combined with warm die compaction in increasing green density, in reducing ejection forces, springback and dimensional changes on sintering [16]. The aim of the present paper is not only to compare bulk lubrication and die wall lubrication, but to further verify the potential of combining die wall lubrication, to maximize green density, with high sintering temperature, to improve the pore morphology. The two available solutions to maximize the fraction of the load bearing section of the materials [17] are combined here.

EXPERIMENTAL PROCEDURE

Transverse Rupture Strength (TRS) specimens, according to the ASTM-B925 (32x12x6 mm) were produced using three commercial water atomized pre-alloyed powders: 1.5%Mo (A), 1.8%Cr (B) and 3%Cr-0.5%Mo (C) with a 0.6% of graphite, using a laboratory mechanical press working in force control with a WC/Co die.

The green specimens were produced with two compaction strategies:

1. bulk lubrication (BL) with 0.7% Acrawax C, warm die compaction at 90°C and 1000 MPa;
2. die wall lubrication (DWL), with a proprietary lubricant, warm die compaction at 90°C and 1000 MPa.

The lubricant used in die wall lubrication is an aqueous suspension of two lubricants; it is sprayed on the die cavity surface and on the surface of the punches every stroke.

The temperature for warm compaction was defined from preliminary studies on cylindrical specimens that highlighted how any increase above 90°C does not result in any significant increase in green density [16].

The green specimens were sintered at 1250°C, 30 minutes isothermal holding, in the graphitic chamber of a vacuum furnace TAV mini-jet with a heating rate of 10°C/min. During the heating step, the specimens were held at 1000°C for 10 min aiming toward homogenizing the temperature. The furnace pressure was set at 0.2 mbar Argon and cooling was carried out in a flowing Nitrogen at 1.5 bar.

Table 1 summarizes the materials investigated with the codes used in the following. For each material, four specimens were produced.

Tab.1. Materials investigated and relevant codes.

Base powder	Additive	Compaction strategy	Code
1.5%Mo	0.6% graphite – 0.7% Acrawax	Bulk lubrication	A-BL
	0.6% graphite	Die wall lubrication	A-DW
1.8%Cr	0.6% graphite – 0.7% Acrawax	Bulk lubrication	B-BL
	0.6% graphite	Die wall lubrication	B-DW
3%Cr-0.5%Mo	0.6% graphite – 0.7% Acrawax	Bulk lubrication	C-BL
	0.6% graphite	Die wall lubrication	C-DW

Specimens have been measured by a digital caliper in the green and sintered state and weighted by an analytical balance "Gibertini E42" (0.0001 g) to determine density.

Three-point bending tests have been performed by a MTS® servohydraulic apparatus. From the load at fracture P_f the *TRS* was determined by eq. (1); from the maximum deflection y_{max} the maximum fracture strain E_f was determined by eq. (2). E_f is the strain experienced at fracture point on the specimen surface subject to tensile load.

$$TRS = \frac{3\,P_f\,L}{2\,w\,t^2} \tag{1}$$

$$E_f = \frac{6\,y_{max}\,t}{L^2} \tag{2}$$

where:
- L is the span length (distance between supports);
- w is the specimen width;
- t is the specimen thickness;

After metallographic preparation, six images at 200x were collected at the Light Optical Microscope (LOM) and processed by "Leica QWin" application to determine the amount, dimension and morphology of the pores.

The equivalent diameter D_{circle}

$$D_{circle} = \sqrt{\frac{4A}{\pi}} D_{circle} = \sqrt{\frac{4A}{\pi}} \tag{4}$$

and the shape factor f_{circle}

$$f_{circle} = \frac{4\pi A}{p^2} f_{circle} = \frac{4\pi A}{p^2} \tag{5}$$

were determined. A is the area of pore and p is its perimeter. f_{circle} expresses the irregularity of the profile of the pores. It tends to 1 in the case of a smooth profile and to 0 for a highly irregular profile. From the distribution of D_{circle} and f_{circle}, 10^{th}, 50^{th} and 90^{th} percentile values were extrapolated. Values of D_{circle} are voluntarily omitted under 2µm in order to avoid all the errors related to the image resolution.

The HV0.1 was measured by carrying out 7 indentations on each specimen.

After metallographic etching with 2% Nital, the microstructure was investigated at the LOM and at the Scanning Electron Microscope (SEM).

RESULTS AND DISCUSSION

The Fig. 1 shows density and relative density for all the materials in the green and the sintered state. The relative densities were calculated with reference to the theoretical

density of the powder mix for the green specimens (including the lubricant in bulk lubrication) and of the steel for the sintered specimens (which does not take into account the lubricant).

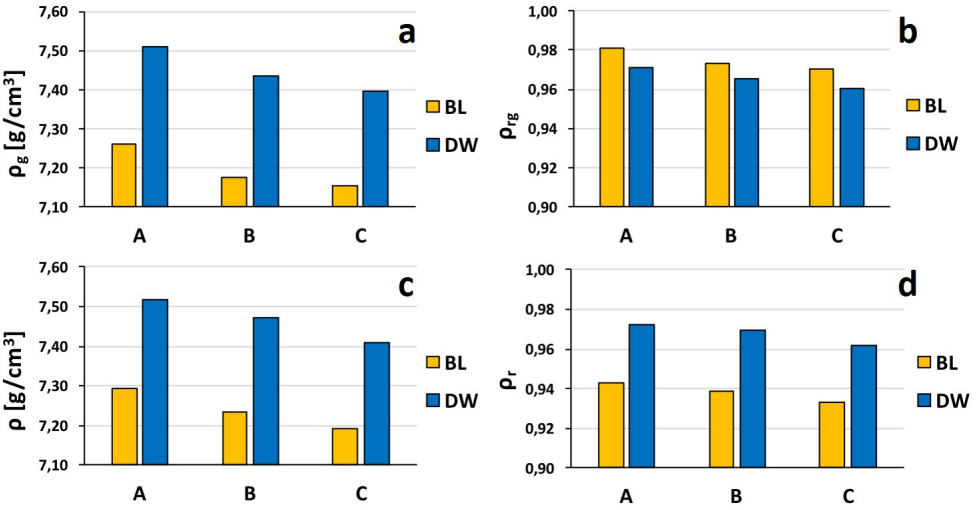

Fig.1. Density and relative densities for all the materials in green (a,b) and sintered (c,d) state.

In BL specimens, the high pressure (1000 MPa) and die temperature (90°C) lead to the achievement of quite a high green density in the three materials, corresponding to 97-98% of the theoretical density of the powder mixes. In DW specimens, green density is lower due to the absence of the lubricant, but relative green density is still 96-97%. The compressibility of the three mixes is different, it decreases from A to B and further to C.

Density slightly increases with sintering, and still decreases from A to B and further to C. The great enhancement of the final density with die wall lubrication is evident in the Figure. The Fig. 2 shows the shrinkage of length (L), width (W) and height (H) of all the materials investigated.

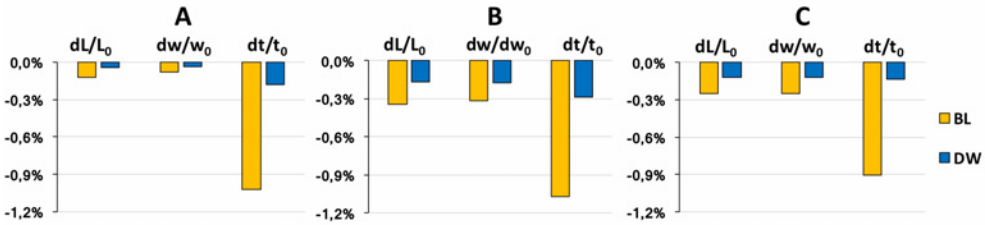

Fig.2. Sintering shrinkage of the materials investigated.

In bulk lubricated specimens, shrinkage of height is much greater than that of dimensions in the compaction plane, highlighting a pronounced anisotropy. In die wall lubricated specimens, shrinkage of the three dimensions is smaller than in the bulk lubricated ones, and anisotropy is greatly reduced (in steel C the dimensional change is almost isotropic). The decrease of shrinkage with die wall lubrication is due to the higher

green density, as expected. The decrease of anisotropy does not have an obvious interpretation. In principle, the absence of lubricant increases the interparticle friction, reducing the radial stress during compaction, which should result in an increased anisotropy of the compaction stresses. This is expected to increase the shrinkage anisotropy [18]. This subject will be investigated in depth in a future work. The Fig. 3 shows examples of the images captured by LOM, one for each sintered specimen.

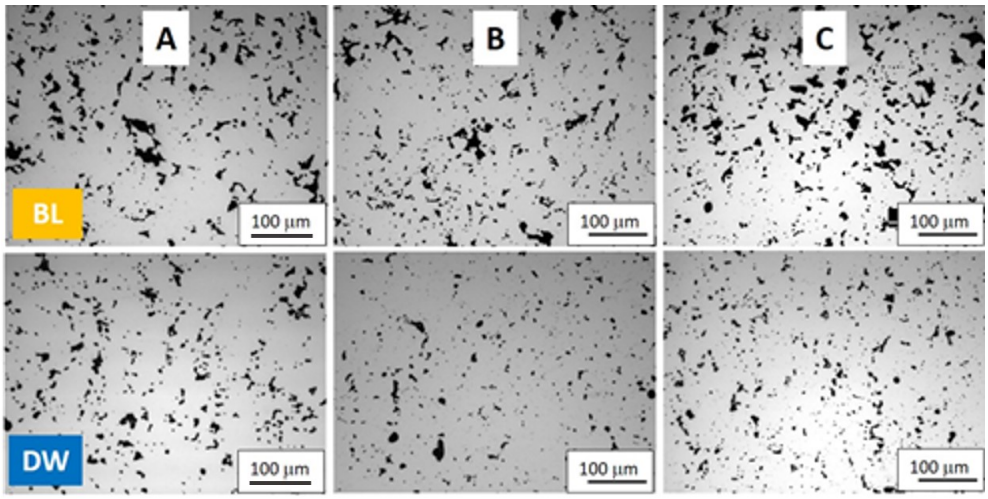

Fig.3. LOM images of sintered specimens.

One can observe the shape of pores with the changing of compaction strategy. The pores of the BL specimens are characterized by very irregular shapes, while those of DW specimens have a more regular and more rounded shape. Another feature highlighted by optical microscopy is the dimension of pores, which decreases from bulk lubrication to die wall lubrication. The Fig. 4 shows D_{circle} distribution for all the studied specimens.

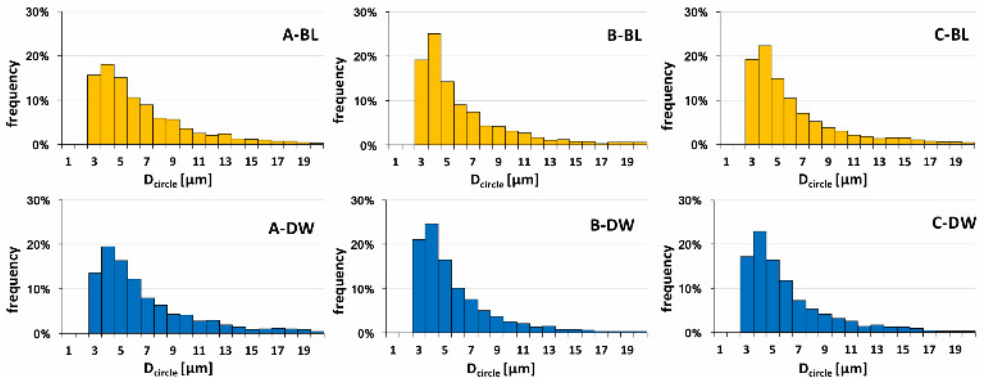

Fig.4. The D_{circle} distribution for all the specimens.

One can qualitatively observe that the distribution tends to move to low values of D_{circle} going from BL to DW and from A to C. In Fig. 5 the median, the 10th and 90th percentiles of D_{circle} distributions are shown for each material.

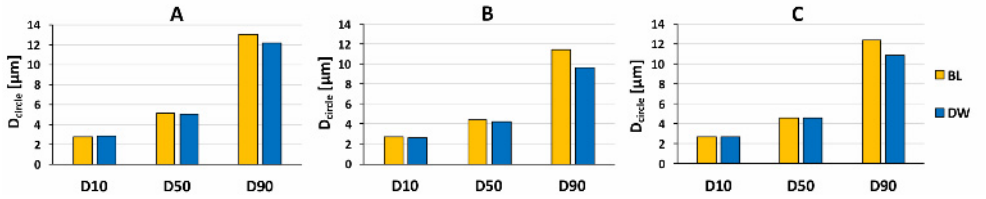

Fig.5. The 10th, 50th and 90th percentile values of the Dcircle distribution.

While the difference among the 10th and 50th percentiles of the equivalent diameters is really small, at 90th percentile the difference becomes greater, indicating that the densification promoted by die wall lubrication mainly affects the larger pores. Figures 6, 7 and 8 show the shape factor fcircle, as a function of Dcircle and the bar diagrams of the 10th, 50th and 90th percentiles.

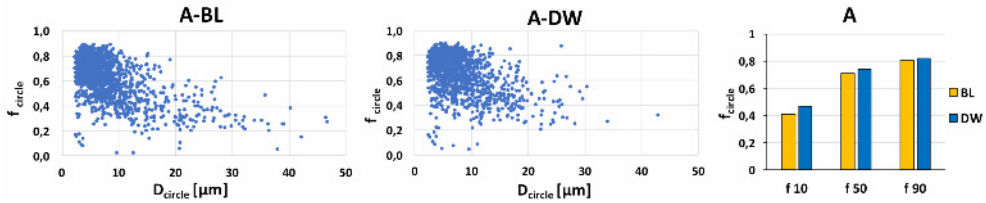

Fig.6. The f_{circle} vs. D_{circle}, and 10th, 50th and 90th f_{circle} percentiles of material A.

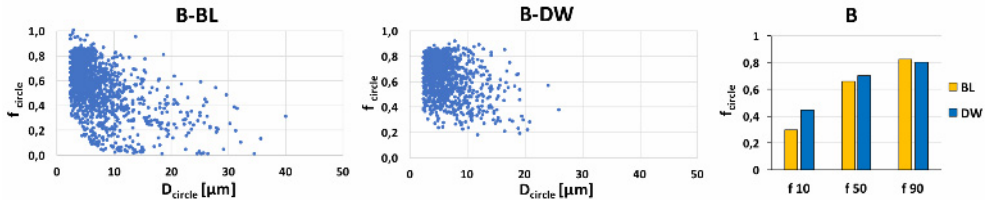

Fig.7. The f_{circle} vs. D_{circle}, and 10th, 50th and 90th f_{circle} percentiles of material B.

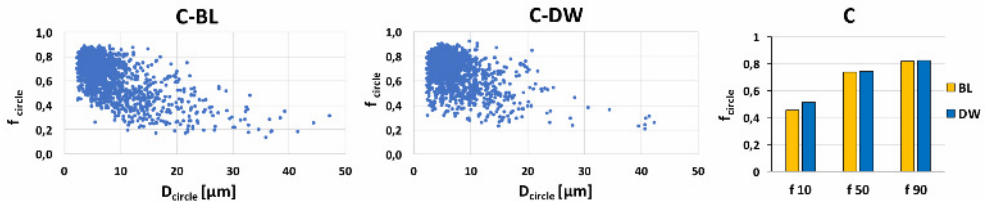

Fig.8. The f_{circle} vs. D_{circle}, and 10th, 50th and 90th f_{circle} percentiles of material C.

Usually, as the dimension of pores increases, f_{circle} gets worse, going to values close to zero. The figures clearly show this trend. The distribution of pores points out the presence of a higher number of large pores in the case of BL specimens for all of three powders, A, B and C. The transverse rupture strength *TRS* and the deformation at fracture E_f are displayed in Fig. 9.

Die wall lubrication, as expected because of the increase in density and the global improvement of porosity, increases TRS and deformation at fracture with respect to bulk lubrication.

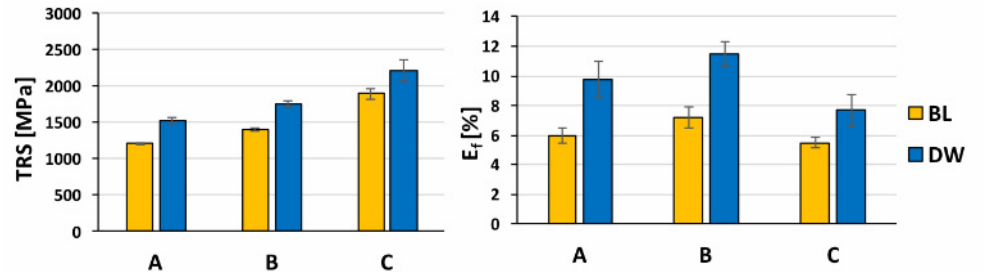

Fig.9. The *TRS* and deformation at fracture deformation E_f.

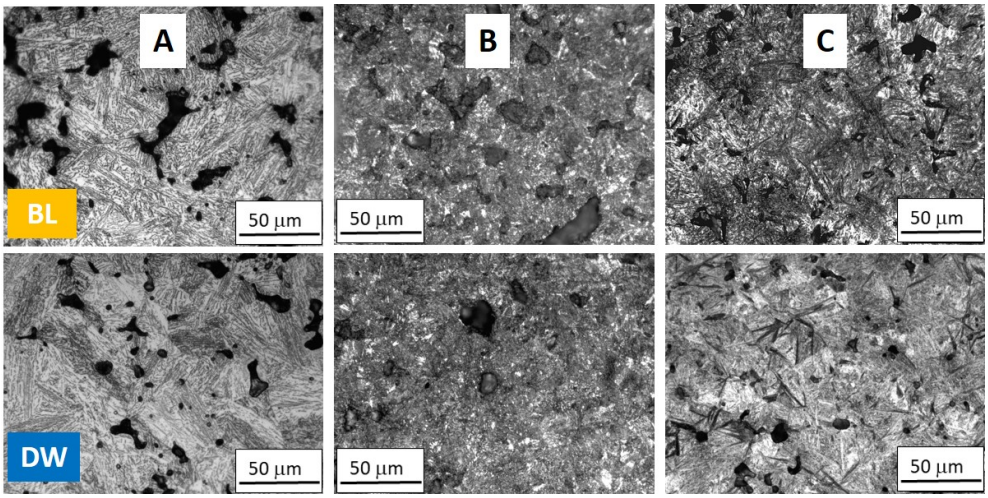

Fig.10. The LOM images of microstructure of the investigated materials.

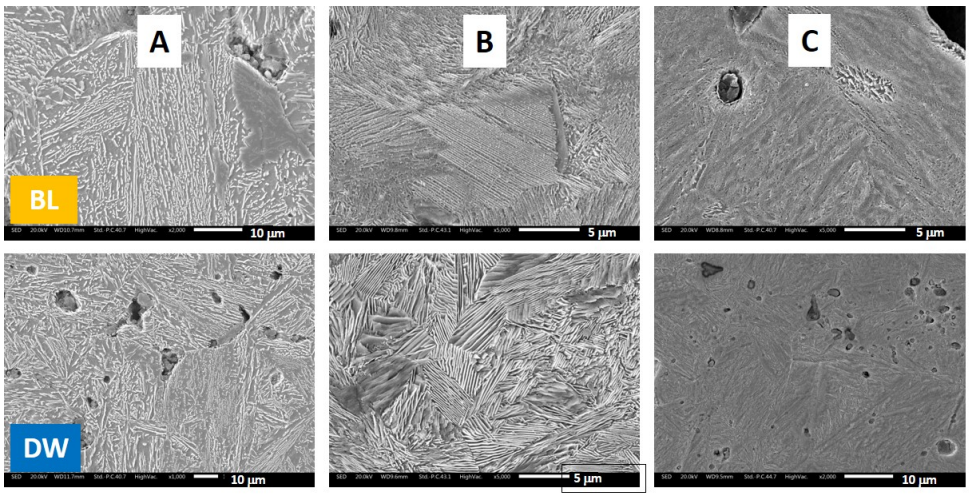

Fig.11. SEM Images of microstructure of the investigated material.

Among the three materials, the 3%Cr steel has the higher TRS and the lowerst deformation at fracture. This result finds an interpretation in the microstructure.

Fig. 10 and 11 show the microstructure of the materials observed by LOM and by SEM, respectively.

Material A has a bainitic microstructure, material B is mostly pearlitic (fine pearlite) with some bainite, material C is almost fully martensitic with some lower bainite shaves. The microstructure does not change with the compaction strategy. The different microstructure affects microhardness, that is reported in Figure 12.

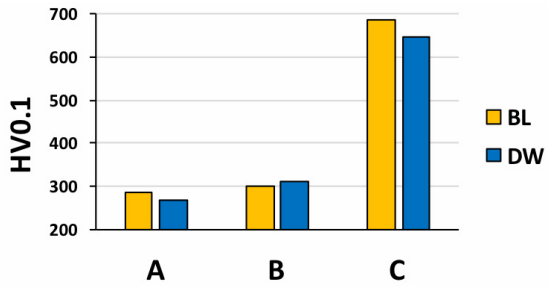

Fig.12. Microhardness of the investigated materials.

The microhardness of material C is the highest, due to the prevailing martensitic microstructure. Due to the presence of bainite, the scatter is quite high (± 40 HV0.1), and therefore the differences between BL and DW are not significant. The bainitic microstructure of material A and the fine pearlitic microstructure with traces of bainite of material B result in a lower microhardness than material C. Again, the differences between BL and DW are not significant since thay are smaller than the scatter band (± 20HV0.1).

CONCLUSIONS

In this paper the influence of die wall lubrication during warm die compaction on densification, microstructure and mechanical properties of three low alloy ferrous powders was investigated.

Transverse rupture strength specimens were produced by two different compaction strategies: bulk lubrication, characterized by conventional lubrication of powder, and die wall lubrication which involves the absence of lubricant in the powder mix. In both cases, compaction was carried out with the die at 90°C. Die wall lubrication leads to higher density for green specimens assuring a higher dimensional stability during sintering. The pores are smaller for die wall compacted specimens, and some of biggest ones are more rounded than in bulk lubricated specimens.

Higher density and better pore morphology result in better TRS and deflection. The compaction strategy does not affect the final microstructure of sintered specimens, which is instead determined by starting powders. The final microstructure has a strong influence on mechanical properties: the material B (1.5%Cr) is the best compromise in terms of transverse rupture strength and fracture strain.

Acknowledgement

The project was carried out in the framework of the Life Green Steel project, LIFE16 ENV/IT/000231.

REFERENCES

[1] Simchi, A., Nojoomi, A.: Advances in Powder Metallurgy and Particulate Materials, vol. 3, 2013, p. 86
[2] Paris, V., Thomas, Y., Francois, P. In: Proceedings EuroPM2015, Reims (F) 4-7 October 2015, Compaction and Lubricants, CD room EPMA, Shrewsbury (UK)
[3] Larsson, M., Knutsson, P. In: Proceedings EuroPM2017, Milan (I) 1-5 October 2017, Compaction, CD room EPMA, Shrewsbury (UK)
[4] Falleur, G., Shah, S., Hanejko, F., Patel, S.: Advances in Powder Metallurgy and Particulate Materials, vol. 3, 2014, p. 117
[5] Paris, V., St-Laurent, S., Thomas, Y.: Advances in Powder Metallurgy and Particulate Materials, vol. 3, 2014, p. 34
[6] Sokolowski, P., Shade, C.: Advances in Powder Metallurgy and Particulate Materials, vol. 3, 2015, p. 40
[7] Knutsson, P., Larsson, M. In: Proceedings EuroPM2014, Salzburg (A) 21-24 September 2014, Compaction, CD room EPMA, Shrewsbury (UK)
[8] James, BA.: Powder Metallurgy, vol. 30, 1987, no. 4, p. 273
[9] Unami, S., Ozaki, Y., Uenosono, S.: JFE Technical Report, vol. 4, 2004, p. 81
[10] Lemieux, P., Gelinas, C.: Advances in Powder Metallurgy and Particulate Materials, vol. 3, 2015, p. 82
[11] Machio, C., Machaka, R., Chikwanda, HK.: Materials and Design, vol. 90, 2016, p. 757
[12] Xiao, ZY., Ke, MY., Fang, L., Shao, M., Li, YY.: Journal of Materials Processing Technologies, vol. 209, 2009, p. 4527
[13] Li, YY., Nagai, L., Zhang, DT., Long, Y., Xia, W.: Journal of Materials Processing Technologies, vol. 129, 2002, p. 354
[14] Korachkin, D., Gathin, DT., Lewis, RW., Tweed, JH.: Powder Metallurgy, vol. 51, 2008, no. 1, p. 14
[15] Babakhani, A., Haerian, A., Ghambari, M.: Materials Science and Engineering A, vol. 437, 2006, p. 360
[16] Zadra, M., Girardini, L., Pederzini, G., Patuelli, G., Piva, M., Bordin, S., De Mitri, L., Popolizio, A., Cristofolini, I., Molinari, A. In: Proceedings EUROPM2018 Congress and Exhibition, Bilbao (Spain), 14-18 October 2018, ed. EPMA, Shrewsbury (UK), CD room
[17] Molinari, A., Menapace, C., Santuliana, E., Straffelini, G.: Powder Metallurgy Progress, vol. 11, 2011, no. 1-2, p. 12
[18] Molinari, A., Amirabdollahian, S., Cristofolini, I.: Advances in Powder Metallurgy and Particulate Materials, vol. 1, 2016, p. 45